When Will MISR Detect Rising High Clouds?

Travis Aerenson[1,1], Roger Marchand[1,1], Hélène Chepfer[2,2], and Brian Medeiros[3,3]

[1]University of Washington
[2]LMD/IPSL Sorbonne Université
[3]National Center for Atmospheric Research

December 1, 2022

Abstract

It is predicted by both theory and models that high-altitude clouds will occur higher in the atmosphere as a result of climate warming. This produces a positive longwave feedback and has a substantial impact on the Earth's response to warming. This effect is well established by theory, but is poorly constrained by observations, and there is large spread in the feedback strength between climate models. We use the NASA Multi-angle Imaging SpectroRadiometer (MISR) to examine changes in Cloud-Top-Height (CTH). MISR uses a stereo-imaging technique to determine CTH. This approach is geometric in nature and insensitive to instrument calibration and therefore is well suited for trend analysis and studies of variability on long time scales. In this article we show that the current MISR record does have an increase in CTH for high-altitude cloud over Southern Hemisphere (SH) oceans but not over Tropical or the Northern Hemisphere (NH) oceans. We use climate model simulations to estimate when MISR might be expected to detect trends in CTH, that include the NH. The analysis suggests that according to the models used in this study MISR should detect changes over the SH ocean earlier than the NH, and if the model predictions are correct should be capable of detecting a trend over the Tropics and NH very soon (3 to 10 years). This result highlights the potential value of a follow-on mission to MISR, which no longer maintains a fixed equator crossing time and is unlikely to be making observations for another 10 years.

Journal of Geophysical Research

Supporting Information for

When Will MISR Detect Rising High Clouds?

Travis Aerenson[1], Roger Marchand[1], Hélène Chepfer[2], Brian Medeiros[3]

[1]University of Washington Department of Atmospheric Sciences

[2]LMD/IPSL Sorbonne Université

[3]National Center for Atmospheric Research, Climate and Global Dynamics

Contents of this file

Text S1 to S4 Figures S1 to S5

Introduction

The supporting information below includes a summary of the climatological biases that are present in the MISR-COSP CTH-OD joint histograms, which shows that there are significant biases in the base-states of CESM2 and IPSL-CM6A-LR. There is also analysis of the decorrelation time for WCTH in different regions, which result in the choice for a 2-year block length in the moving block bootstrap described in the main text. Also included is an analysis of how the MISR discretization would affect a narrowly distributed cloud layer. Finally, there are the results of how changes to the MISR Equator crossing time will influence the CTH retrievals. Additional description and analysis can be found in the accompanying thesis work:

Aerenson, T. (2021). When Will MISR Detect Rising High Clouds?*Master of Science Thesis University of Washington* .

Text S1.

MISR Simulator Base State Climatology

This section of the supplement is dedicated to understanding how the mean cloud climatology or base state of the models differs from observations. Here and in later analysis, the MISR output is averaged over 5 latitude bands: Tropics -20° to 20°, Subtropics ±20° to ±40°, and Midlatitudes ±40° to ±60°. The mean CTH-OD histogram observed by MISR, along with simulated histograms for CESM2 and IPSL SSP 585 simulations are shown in **Figures S1 and S2** . All three histograms are averages taken over the period 2001 to 2015, which is the portion of the SSP 585 simulation that is based on historical emissions (rather than projected emissions) that overlaps with the MISR record. The MISR observations are restricted to ocean, and the model averages are restricted to ocean to match.

Figure S1 shows that distribution of clouds in CESM2 and IPSL differ noticeably between each other and with the observations. Of particular note is that IPSL does not produce much mid-level cloud (between 5 and 7 km), which have a cooling effect on the tropical climate (Bourgeois et al., 2016), and produces more optically thin high clouds (OD less than 3.6) than is observed by MISR. In contrast, CESM2 has more mid-level clouds and has more high cloud with optical depths between 1.3 and 23 than observations. In both models high clouds are predominantly located between 11 and 13 kilometers (in agreement with observations), but the observed distribution is wider, with more cloud occurring outside of the 11-13 km bin, than the models (especially IPSL). The thin distribution of IPSL has implication for our WCTH that are discussed below.

The histograms averaged over the subtropics and midlatitudes are shown in **Figure S2** . Total cloud occurrence in the subtropics (20^o to 40^o) is dominated by low clouds, with much less high and mid-level clouds as compared to the tropics. High clouds are lower in altitude and optically thinner on average than in the tropics. The most occupied vertical bin is between 9 and 11 km in the Norther Hemisphere (NH) and 7 to 9 km in the Southern Hemisphere (SH). In both models and observations there are fewer optically thin clouds above 5 km in the SH than in the NH.

In the midlatitudes the cloud patterns are dominated by midlatitude cyclones. Optically thick high clouds occur lower in the atmosphere than in the subtropics or tropics in both observations and models. The presence of a mid-level cloud peak remains visible in the MISR observations and CESM2 simulations, located in the 3 to 4 km height bin. In IPSL, high clouds are optically thicker than observations, with a significant fraction of high clouds having optical depth greater than 60.

Bourgeois, Q., Ekman, A. M. L., Igel, M. R., & Krejci, R. (2016). Ubiquity and impact of thin mid-level clouds in the tropics.*Nature Communications* , *7* (1), 1–6. https://doi.org/10.1038/ncomms12432

Text S2.

Autocorrelation of WCTH

Much of the autocorrelation in WCTH is dominated by the ENSO cycle, which has been found to have decorrelation times between 6 and 10 months (Berner et al., 2020; Burgers & van Oldenborgh, 2003). Autocorrelation functions of WCTH are shown in **Figure S3** where it can be seen that in each of the five latitude bands the autocorrelation is well below the e-fold point (indicated by the red line) within 12 months lag.

Sensitivity tests were performed to determine what block length is acceptable. In the tropics the moving block resampling scheme was applied to the WCTH averaged over the tropics (the region with the latest decorrelation) using 6-, 12-, 24-, and 48-month block lengths. There is no significant difference using a block length of 24 or 48 months, however results based on lengths below 24 months differ substantially, and so a block length of 2 years was used for all results shown in the main text.

Berner, J., Christensen, H. M., & Sardeshmukh, P. D. (2020). Does ENSO regularity increase in a warming climate? *Journal of Climate* ,*33* (4), 1247–1259. https://doi.org/10.1175/JCLI-D-19-0545.1

Burgers, G., & van Oldenborgh, G. J. (2003). On the impact of local feedbacks in the central Pacific on the ENSO cycle. *Journal of Climate* , *16* (14), 2396–2407. https://doi.org/10.1175/2766.1

Text S3.

Understanding the "Faster than FAT" Response in the Tropics of IPSL

To determine if the "Faster than FAT" response in IPSL may be an effect of the MISR discretization we investigate how a "thin" distribution of high clouds appears to move upward given the MISR grid discretization. Specifically, we assume a gaussian distribution for the vertical profile of high clouds (**Figure S5**). We find that if the width (standard deviation) of the underlying CTH distribution is 700 m or larger, then the WCTH captures the increase in CTH well. However, if the width is less than 700 m (400 m is used in the example in**Figure S5**), the MISR discretization poorly captures the slow rise in the peak position of the distribution (left panel) and WCTH can appear to rise faster or slower than the true peak depending on whether the true peak is above or below the bin mid-point; and in the limit where there is no width in the distribution (meaning all CTH occurs at a single fixed height), the WCTH would appear as a flat except for a single step of 2 km (the size of the MISR vertical bins) as the CTH moves from one MISR bin to the next. In **Figure S5** a gaussian distribution of CTH with a width of 400 m is slowly lifted with the position of the peak moving from 12 to 14 km (top right panel) and the resulting MISR CTH distribution and WCTH are shown in the top left panel and bottom left panels, respectively. The bottom right plot is designed to mimic the results produced by tropical cloud in IPSL by adding white noise to the position of the Gaussian peak. In summary, IPSL has a narrow high cloud distribution in the tropics, the rapid rise in WCTH seen in IPSL after 2040, and slow down after 2060, as well as the increased variability between 2040 and 2060 (as seen in **Figure 7** of the main text) are consistent with how a narrow cloud distribution would be seen by the MISR simulator. It is noted that if the distribution of CTH in the real world were as narrow as suggested by the IPSL model, the WCTH based on the MISR observations would have this same undesirable property. However, that does not appear to be the case (as can be seen in **Figure S1** , as observed high cloud is spread across several MISR height bins). Of course, it is worth noting that the MISR retrievals have some random error associated with them (largely due to uncertainty in wind correction, see Marchand et al. 2010), which will cause the observed distribution to be broader than the true distribution. Given the potential for artifacts, it might be wise to increase the resolution of the MISR CTH-OD product and simulated output, in the future.

Text S4.

Derivation of additional variance due to MISR sampling.

Let the variance be estimated using the following unbiased estimator

$$S^2 = \frac{1}{n-1}\sum_i \left(x_i - \frac{\sum x}{n}\right)^2 \text{(S1)}$$

where x_i are sampled values. As proven by Cho 2004 (Corollary 1), Cho and Cho 2008 (Eq. 1), and Behnhmou

(2018 Equations. 10 and 11), the variance of the variance of a sampled population with the above estimator and a large number of samples (n) can be approximated as,

$$\mathrm{var}\left(S^2\right) \approx \frac{1}{n}\left(\mu_4 - \frac{n-3}{n-1}(\mu_2)^2\right) \text{(S2)}$$

where $\mu_n = \mathrm{E}[(\mathrm{X} - \mathrm{E}(\mathrm{X})^{\mathrm{k}}]$ is the n-th order moment and E the expected value. For a Gaussian distribution the 4th moment is given by $\mu_4 = 3\sigma^4$ and the 2^{nd} moment is the variance $\mu_2 = \sigma^2$, and yields the results that

$$\mathrm{var}\left(S^2\right) = \frac{2\sigma^4}{n-1}. \text{ (S3)}$$

Thus the measured sampled variance (S^2) will be given by true variance of the sample population (σ^2), because the estimator is unbiased, with one standard deviation given by the square root of the above variance,

$$S^2 = \sigma^2 \pm \sqrt{\frac{2\sigma^4}{n-1}} = \sigma^2\left(1 \pm \sqrt{\frac{2}{n-1}}\right). \text{ (S4)}$$

And the measured standard deviation (S) becomes,

$$S = \sigma\sqrt{1 \pm \sqrt{\frac{2}{n-1}}}\,. \text{ (S5)}$$

Expanding the square root in a taylor series ($\sqrt{1+x} \approx 1 + \frac{1}{2}x +$ higher order terms), yields

$$S \approx \sigma\left(1 \pm \frac{1}{2}\sqrt{\frac{2}{n-1}}\right) = \sigma \pm \frac{\sigma}{\sqrt{2n-2}} \text{ (S6)}$$

with the increase in the standard deviation (relatively to that of the unsampled population) given by the second term in S6. Note this is the one-sigma uncertainty. While equation S6 was derived assuming Gaussian statistics, as equation S2 shows, in general the variance (of the variance) is proportional to 1/n and consequently for any reasonable distribution (one with finite moments) the standard deviation of the sampled population will asymptotically approach the true standard deviation proportional to $1/\sqrt{n}$. In numerical test with Gaussian distributions, we find Eq. S6 is quite a good approximation (error of only a few percent), even for values of n as small as 10.

Cho, E. (2004). The Variance of Sample Variance for a Finite Population.*ASA Section on Survey Research and Methods* , 3345-3350

Cho, E. and Cho, M.J. (2008). Variance of sample variance. *Section on Survey Research Methods–JSM* , *2* , pp.1291-1293.

Benhamou, E. (2018). A few properties of sample variance. *arXiv preprint arXiv:1809.03774* .

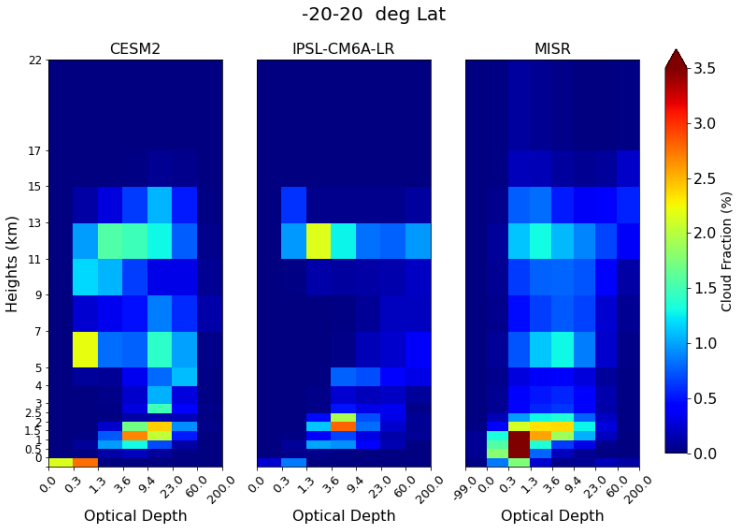

Figure S1 . Observed and simulated MISR CTH-OD histograms, tropical ocean (-20° to 20°latitudes), for the period of 2001-2015. In the MISR observations the leftmost OD range indicates when MISR was unable to determine the correct OD of the cloud, but was able to determine that cloud occurred at that height

Hosted file

`image3.emf` available at https://authorea.com/users/560048/articles/608284-when-will-misr-detect-rising-high-clouds

Figure S2. Same as **Figure S1** only averaged over subtropics and midlatitudes

Figure S3. Autocorrelation functions of WCTH shown for the observations as well as the two models in each of the five latitude bands. Only the historical period is considered of the model simulations to be comparable with observations. Red lines indicate 1/e so that decorrelation time is the number of lags required to cross the red line

Figure S4. The impact of Equator Crossing Time on WCTH is shown as the monthly anomaly WCTH caused by changes in ECT for each model, and at each latitude range. The bottom row depicts the multi-model mean

Hosted file

`image6.emf` available at https://authorea.com/users/560048/articles/608284-when-will-misr-detect-rising-high-clouds

Figure S5 Top: Vertical distribution of cloud occurrence modeled in the right panel as a Gaussian profile with a width of 400 m and where the cloud layer peak moves from 12 to 14 km, and in the left panel showing the resulting MISR discretization. Bottom: WCTH calculated from gaussian model before and after it is aggregated into discrete bins with 200-time steps. Left plot has the CTH maximum going from 12 to 14 km. The right plot is designed to most closely mimic the results of IPSL, where peak cloud occurrence goes from 12.5 to 14.5 km, and has noise added to the profile to emulate the impact of internal variability on the cloud fraction profile.

When Will MISR Detect Rising High Clouds?

Travis Aerenson[1], Roger Marchand[1], Hélène Chepfer[2], and Brian Medeiros[3]

[1]University of Washington, Department of Atmospheric Sciences

[2]LMD/IPSL, Sorbonne Université

[3]National Center for Atmospheric Research, Climate and Global Dynamics

Corresponding author: Travis Aerenson (aerenson@uw.edu)

Key Points:

- The current MISR observational record shows an increase in cloud-top-height (CTH) of high cloud over the Southern Hemisphere Oceans.
- Climate models suggest rising CTH due to climate warming will be globally observable in the near future if model predictions are correct.
- Models with higher ECS have more rapidly rising high-clouds, but this does not always lead to an earlier observable trend.

Abstract

It is predicted by both theory and models that high-altitude clouds will occur higher in the atmosphere as a result of climate warming. This produces a positive longwave feedback and has a substantial impact on the Earth's response to warming. This effect is well established by theory, but is poorly constrained by observations, and there is large spread in the feedback strength between climate models. We use the NASA Multi-angle Imaging SpectroRadiometer (MISR) to examine changes in Cloud-Top-Height (CTH). MISR uses a stereo-imaging technique to determine CTH. This approach is geometric in nature and insensitive to instrument calibration and therefore is well suited for trend analysis and studies of variability on long time scales. In this article we show that the current MISR record does have an increase in CTH for high-altitude cloud over Southern Hemisphere (SH) oceans but not over Tropical or the Northern Hemisphere (NH) oceans. We use climate model simulations to estimate when MISR might be expected to detect trends in CTH, that include the NH. The analysis suggests that according to the models used in this study MISR should detect changes over the SH ocean earlier than the NH, and if the model predictions are correct should be capable of detecting a trend over the Tropics and NH very soon (3 to 10 years). This result highlights the potential value of a follow-on mission to MISR, which no longer maintains a fixed equator crossing time and is unlikely to be making observations for another 10 years.

Plain Language Summary

There is a feedback to climate change associated with high-altitude clouds rising higher up in the atmosphere that is predicted by physical theory to enhance warming, and is found in a wide range of models. To date, there is little observational evidence for rising high clouds. An observation of a trend in cloud-top-height (CTH) in the atmosphere would enhance our understanding of this feedback, and climate warming as a whole. This study uses the Multi-angle Imaging SpectroRadiometer (MISR) to examine changes in CTH. Currently the MISR observational record does show a trend in CTH over the Southern Hemisphere (SH) oceans, but does not show a trend over the Tropical or the Northern Hemisphere (NH) oceans. We use model simulations to examine how long it should take for MISR to observe trend changes in CTH that include the Tropics and NH. The models used in this study suggest that MISR should be capable of observing a trend in the next 3 to 10 years. MISR is unlikely to be making measurements suitable for this kind of trend analysis for another 10 years, and this highlights the value of a follow-on mission to MISR which can extend the stereo-imaging record.

1. Introduction

Clouds play an important role in the Earth's radiation budget. They simultaneously cool the Earth by reflecting shortwave sunlight, and insulate the Earth by reducing longwave emission to space. Cloud feedbacks (changes in cloud properties as a result of temperature change that in turn either enhance or diminish the temperature change) are important to understanding the future climate (Schneider, 1972; Stephens, 2005; Webb et al., 2017). Cloud feedbacks remain one of the largest causes of uncertainty (spread) in climate model projections (Soden & Held, 2006; Zelinka et al., 2020). The amplitudes and sign of many cloud feedbacks vary among climate models. One cloud feedback on which there is broad agreement, however, is that the cloud-top-height (CTH) of high clouds at all latitudes will experience an upward shift in altitude as the surface and troposphere warm. An increase in CTH with warming has been seen in climate simulations dating back to the 1980s (Hansen, 1984; Wetherald & Manabe, 1988), and remains a robust feature in modern cloud resolving models and climate model simulations (Harrop & Hartmann, 2012; Kuang & Hartmann, 2007; Zelinka et al., 2013).

This effect is a well understood response to warming, explained by the Fixed Anvil Temperature (FAT) hypothesis: which asserts that the height at which high-altitude anvil clouds form is nearly fixed in temperature and is independent of surface temperature (Hartmann & Larson, 2002; Zelinka & Hartmann, 2010). Anvil temperature is nearly fixed because anvils form where latent heating by condensation balances clear-sky longwave radiative cooling. The vertical profile of clear-sky longwave cooling is largely controlled by the vertical distribution of water vapor. The Clausius-Clapeyron equation shows that when the atmosphere is near saturation (which on large scales is typically a good approximation), the water vapor content decreases quasi-exponentially with temperature. Consequently, at sufficiently cold temperatures, there is insufficient water vapor to significantly cool the atmosphere through thermal emission to space (as compared with the warmer and moister atmosphere below) and the rapid decrease in water vapor effectively sets a preferential temperature for the top of the longwave cooling profile (and consequently anvil cloud formation). A slightly altered version of the FAT hypothesis (known as the proportionately higher anvil temperature hypothesis or PHAT) was developed by Zelinka & Hartmann (2010), which asserts that the preferential temperature for anvil tops will warm slightly (i.e. cloud top does not remain truly fixed in temperature) because there will be larger static stability in the upper atmosphere. This results in anvil clouds rising in the atmosphere, but at a slower rate than required to remain at a constant temperature. We note the spectroscopy of water vapor (the change in opacity of water vapor with frequency and pressure that arises from the quantum mechanical properties of water vapor molecules) plays a critical role in the radiative cooling profile. Cooling is not restricted to a narrow band near the top of the water-vapor profile, but cooling is distributed throughout the depth of the troposphere and helps set this critical temperature where the longwave cooling "kinks" at around 220 K (Jeevanjee & Fueglistaler, 2020).

Rising CTH with a fixed anvil temperature creates a positive feedback on climate, because while the surface warms and longwave emission to space increases from the surface, the emission temperature of anvil cloud changes very little. So, more heat is held by the Earth system than if anvil temperatures warmed proportionally to the surface temperature. Of course, reduction in high cloud area or thickness (opacity to infrared) could offset the change in CTH, and this possibility remains a topic of considerable interest (Bony et al., 2016). Nonetheless, rising CTH creates a positive longwave feedback. We also note that while the FAT hypothesis was originally developed for tropical anvil clouds, changes in the clear-sky radiative cooling

profiles are likewise expected in midlatitudes, and the theory that anvil cloud height follows the clear-sky radiative cooling profile appears to hold well in the midlatitudes (Thompson et al., 2017).

Interestingly, there has been evidence that the tropopause may increase in altitude in a way that is fixed in temperature (Seeley et al., 2019). It has long been understood that the tropopause (and associated thin clouds) will increase in height with climate change (Hu & Vallis, 2019; Vallis et al., 2015; Zhou et al., 2014), but it is a relatively new result that the tropopause may be tightly linked to the temperature profile. Seeley et al. (2019) identified this behavior based on model simulations, and the physical mechanisms are yet to be established.

Regardless of the physical mechanisms responsible for rising CTH, the associated LW feedback is produced consistently in models, but it's contribution to the global energy budget varies from model to model. Thus, it is important to study and understand this positive feedback mechanism. Satellites provide a particularly advantageous position for observing cloud-top, and satellite measurements could potentially be used to evaluate or constrain model simulations of cloud-top-height.

To date there is little evidence in the observational record for increasing cloud-top-height of high cloud. Norris et al. (2016) used the International Satellite Cloud Climatology Project (ISCCP) and Extended Pathfinder Atmospheres (PATMOS) infrared satellite records to examine how zonally averaged cloud profiles have changed between the decades of the 1980s and the 2000s. Norris et al. (2016) found that the ISCCP and PATMOS zonal mean cloud amounts increased in the 50-180 hPa interval and decreased in the 180-310 interval during the period 1983-2009 in the tropics, which is consistent with a rise in the tops of the highest clouds. However, no estimate of the rate of CTH increase was made. Further, the reliability of the ISCCP/PATMOS satellite record is a concern, as the ISCCP/PATMOS record uses many satellites/sensors whose number and position have changed over time, and in general are not calibrated consistently. The infrared retrieval technique for CTH is sensitive to changes in cloud emissivity, view angles, and calibration (Rossow et al., 1993). More recently, Saint-Lu et al. (2020) used a decade-long observational record from the Cloud-Aerosol Lidar and Infrared Pathfinder Satellite Observations (hereafter CALIPSO) to show that anvil clouds form higher in the atmosphere (and decrease in coverage) during warm periods on interannual timescales. Nonetheless, there remains a strong need to understand and quantify CTH trends.

There have been a small number of studies which use satellite simulators embedded into climate models to determine when we will be capable of constraining the rate of rising CTH (and thus the associated feedback) (Chepfer et al., 2018; Chepfer et al., 2014; Takahashi et al., 2019). Two such studies, Chepfer et al. (2018, 2014) (hereafter C18, and C14) made use of a CALIPSO simulator in AMIP (Atmospheric Model Intercomparison Project) and AMIP+4K simulations to estimate how long of a CALIPSO record might be required to observe trends in CTH. C14 focused on tropical high clouds (but also looked at other regions), and used a linear assumption of global warming from the current temperatures to a +4K world over a 100 year period. They found that the CALIPSO record would need to be 15-30 years past the start of the model simulation (2008) to detect a climate trend. Based on output from two climate models, C18 found that a 27-year data record would be needed to distinguish differences in the rate of change in CTH between the two models with 70% confidence. Takahashi et al., (2019) (hereafter T19) used a fully coupled simulation from CESM1 (Community Earth System Model version 1) running the Representative Concentration Pathway 8.5 scenario with 8.5 W/m^2 of radiative forcing at 2100 (RCP 8.5), to determine when CloudSat (or a similar spaceborne radar) would be

capable of observing a climate trend in CTH. This simulation included output from the COSP Quickbeam radar simulator (Bodas-Salcedo et al., 2011). They forecast that a confident (95%) detection based on CloudSat would occur in the mid to late 2020s and would be first detected at latitudes between 20° and 60° in each hemisphere.

Here we undertake a similar analysis to T19 to determine when rising CTH will be detectable with high confidence, but focus on detectability based on CTH from a stereo-imaging technique, which follows that used by the Multi-angle Imaging Spectroradiometer (MISR) instrument (Marchand et al., 2007). In doing so we make extensive use of MISR simulator output (Marchand & Ackerman, 2010; Swales et al., 2018). The stereo-imaging technique employed by MISR uses nine cameras to collect images of the Earth from nine different view angles as the satellite moves along a sun synchronous orbit (Diner et al., 1998). MISR determines cloud-top-height (CTH) using stereo-image parallax, a geometric calculation which is independent of image calibration (Marchand & Ackerman, 2010; Marchand et al., 2007; Moroney et al., 2002).

MISR CTH retrievals have been compared to heights obtained from ground-based and spaceborne radar and lidar and were found to produce very reliable cloud-top-height measurements for cloud with optical depth greater than 0.3 (Hillman et al., 2017; Marchand et al., 2007). Knowing this, and that MISR has a relatively long continuous data record (roughly 20 years), it is clear that MISR is a good candidate for detecting and quantifying any climate trend in CTH.

Our analysis is largely based on output from two climate models running the fifth Shared Socio-economic Pathway with 8.5 W/m^2 of forcing at 2100 (SSP5-8.5) simulation, specifically we use output from the Community Earth System Model version 2 (CESM2) and the latest climate model from Institute Pierre-Simon Laplace (IPSL-CM6A-LR). We also extrapolate results based on a larger collection of models that have run the MISR simulator in AMIP simulations, which are simulations performed using atmospheric models with prescribed the sea-surface temperature (SST) to match with the historical record. Synthetic climate warming projections are made using the SSP5-8.5 scenario temperature outputs and AMIP MISR simulator profiles, assuming the MISR CTH will increase at a rate following the FAT hypothesis.

In this article, the data and methods used for the CTH trend emergence analysis are described in Section 2, which is followed in Section 3 by the time of emergence results for CESM2 and IPSL-CM6A-LR. Section 4 is dedicated to determining how the rising CTH in these models compares to a rate that would be predicted by the FAT hypothesis, after which in Section 5 we use the FAT hypothesis to synthesize how a larger multi-model ensemble might behave, and how CTH trend emergence is different in models with different warming rates. Finally, Section 6 summarizes results and presents the main conclusions.

2. Data and Methods

MISR is aboard the Terra satellite, which is in a sun synchronous orbit with an equator crossing time of about 10:30 am. The instrument consists of nine cameras which view the Earth at nine different angels: nadir plus 26.1, 45.6, 60.0, and 70.5 degrees forward and aft along the direction of flight. Radiance measurements (images) are collected in four narrow spectral bands centered at 443, 555, 670, and 865 nm with a horizontal grid spacing of 275 m to 1.1 km depending on the camera and wavelength (Diner et al., 1998). The MISR CTH-OD dataset used in this study is based on stereo heights derived on a 1.1 km grid (using image matching

techniques) and optical depths retrieved from the observed visible radiances assuming a single layer one-dimensional cloud with a fixed effective radius and no aerosols (Marchand et al., 2010). This study uses version 7 (V7) of the MISR cloud-top-heights optical depth (CTH-OD) product. V7 includes updates to the MISR stereo-retrieval algorithm which have more accurate corrections for cloud horizontal motion based on an updated wind-retrieval algorithm. Details on the updated wind-retrieval algorithm are described by Mueller et al. (2017).

As was found by Marchand (2013), Davies et al. (2017), and will be shown in Section 3, examination of MISR derived cloud-top-heights do not reveal any trends in globally averaged or tropical CTH (although it does now show statistically significant trends in the Southern Hemisphere). This is not a surprise, because as will be shown later, the size of the expected change in CTH to date is small relative to internal variability, and a primary objective of our analysis is to determine when model predicted changes could be detected with high confidence. The MISR simulator, hereafter referred to as MISR-COSP (because it is part of the Cloud feedback model intercomparison project Observation Simulator Package (COSP) that is being run by many modeling centers) is used to produce a MISR-like cloud field that is consistent with the treatment of radiation in each model (Swales et al., 2018). Details on the MISR simulator can be found in Marchand et al. (2010) and Marchand & Ackerman (2010) with evaluation of both MISR observations and MISR-COSP output against CloudSat and CALIPSO (radar and lidar) given by Hillman et al. (2017). Currently the MISR CTH-OD dataset is only generated over ocean, and for comparison MISR-COSP output is restricted to oceans. Similarly, the MISR-COSP only records cloud in the portion of the globe that is sunlit, because MISR is only capable of observing cloud on the daytime portion of its orbit.

We examine trend detectability in the context of model simulations based on the fifth Shared Socioeconomic Pathway scenario with 8.5 W/m^2 of radiative forcing (SSP5-8.5) (O'Neill et al., 2016). In this simulation CO_2 and aerosol emissions are set based on observations from 1850 to 2015 before being allowed to increase until the end of the simulation at 2100. The increase in emissions represents a future with unmitigated emissions, and the implications of this are discussed in the concluding material. As part of the Coupled Model Intercomparison Project phase 6 (CMIP6), two modeling centers produced MISR-COSP outputs for SSP5-8.5 simulations, specifically, data is available from the CESM2 and IPSL-CM6A-LR models. Hereafter the IPSL-CM6A-LR model simulation will be identified as simply IPSL. The SSP5-8.5 simulation is initialized from the historical run. Thus, we concatenate the SSP5-8.5 simulation output onto the historical simulation output to create model time series that begin in 2000 and continue past 2015 and into the future based on projected emissions.

In addition, several models have run the MISR-COSP simulator as a part of the Atmospheric Model Intercomparison Project (AMIP), which are atmosphere only model simulations that have sea-surface temperatures prescribed to closely match the historical temperatures from 1979 to the near present (Gates et al., 1999). Many such models did not generate MISR-COSP output for their SSP5-8.5 simulations. In the analysis we use the MISR-COSP output from the AMIP run in conjunction with the SSP5-8.5 simulated temperature and geopotential profiles to examine CTH detection under the assumption of a FAT-like increase in CTH in these models. Specifically, synthetic MISR projections are produced for CESM2 and IPSL (for comparison with direct MISR simulator output), as well as MRI-ESM2-0, CanESM5, CNRM-CM6-1, CNRM-ESM2-1, and BCC-CSM2-MR. Primary references for each of these models is given in **Table 1**. In the following analysis, these data are first deseasonalized (by subtracting the mean seasonal cycle from the full length of each dataset).

Model	Simulations used	Reference
CESM2	Historical, (MISR-COSP, ta, zg) SSP5-8.5, (MISR-COSP, ta, zg) AMIP (MISR-COSP, ta, zg)	Danabasoglu et al. (2020)
IPSL-CM6A-LR	Historical, (MISR-COSP, ta, zg) SSP5-8.5, (MISR-COSP, ta, zg) AMIP (MISR-COSP, ta, zg)	Boucher et al. (2020)
BCC-CSM2-MR	Historical (ta, zg), SSP5-8.5 (ta, zg), AMIP (MISR-COSP, ta, zg)	Wu et al. (2019)
CanESM5	Historical (ta, zg), SSP5-8.5 (ta, zg), AMIP (MISR-COSP, ta, zg)	Swart et al. (2019)
CNRM-CM6-1	Historical (ta, zg), SSP5-8.5 (ta, zg), AMIP (MISR-COSP, ta, zg)	Voldoire et al. (2019)
CNRM-ESM2-1	Historical (ta, zg), SSP5-8.5 (ta, zg), AMIP (MISR-COSP, ta, zg)	Séférian et al. (2019)
MRI-ESM2-0	Historical (ta, zg), SSP5-8.5 (ta, zg), AMIP (MISR-COSP, ta, zg)	Yukimoto et al. (2019)

Table 1 *A summary of the models used in this analysis. MISR-COSP indicates the simulations with MISR simulator output, ta and zg indicate those where the atmospheric temperature and geopotential fields are used respectively.*

The model AMIP output used here are available for download through the ESGF CMIP6 database (https://esgf-node.llnl.gov/projects/cmip6/) and MISR observation data are available from the NASA Langley archive (http://asdc.larc.nasa.gov/project/MISR/). The SSP5-8.5 simulation with the MISR-COSP simulator was performed as an independent run by each modeling center, and is available at: https://atmos.uw.edu/~roj/MISR_observations/.

2.1 The Weighted Cloud Top Height (WCTH) Metric

MISR and the MISR simulator parse cloud occurrence into a fixed set of CTH and (total column) optical depth bins. To assess a trend in CTH, we calculate a cloud-fraction weighted average CTH (WCTH) from the histogram data as given below in Equation 1. Here we define high clouds as those above 9 km in the tropics (between -20º and 20º latitude), above 7 km in the subtropics (±20º to ±40º latitude), and above 5 km for all latitudes poleward of ±40º in both hemispheres. The MISR histogram is first integrated over (some desired range of) optical depth to obtain the cloud occurrence (CF_z) associated with each MISR height bin (with height CTH_z).

$$WCTH(t) = \frac{\sum_{z>thresh}(CTH_z \times CF_z(t))}{\sum_{z>thresh}(CF_z(t))} \quad (1)$$

The WCTH describes the average height of high clouds, when a high cloud is present, and is independent of the total amount of high cloud (and is conceptually similar to the weighted cloud height (WCH) metric from T19). The altitude thresholds chosen above align with bin boundaries used in the MISR histogram and capture the peak in high-cloud occurrence (Aerenson, 2021; Marchand et al., 2010), and are high enough to avoid issues related to mid-level clouds. Specifically, the rate of change of the CTH of mid-level clouds may not be the same as high clouds, and at a practical level, clouds crossing the threshold – whether it is low-level clouds shifting into mid-levels or mid-level clouds into high-levels can create artifacts in the WCTH metric The thresholds were hand-selected by manually examining the changes in the MISR histograms and selecting the lowest CTH boundaries that avoid the upward motion of mid-level clouds. For the time window examined here (less than 100 years simulated) the hand-selected static thresholds work well, but could become a problem in longer simulations where further warming could cause mid-level clouds to rise past the current thresholds. In the analysis WCTH is calculated over various bands of latitude, and different regions are examined in an effort to determine where MISR will first be able to observe a climate trend as temperature may increase at different rates in different regions, which may lead to different times of emergence.

Of course, not all high cloud are anvils or are related to anvils, which is the focus of the FAT hypothesis. Except where otherwise stated, the WCTH is calculated using all clouds that are observed by MISR (with OD > 0.3), and the WCTH metric is certainly influenced by what is and what is not detected. In the Tropical Western Pacific for example, optically thin cirrus (typically subvisual cirrus with an optical depth less than 0.3) are ubiquitous near the tropopause (in the tropical transition layer). But high clouds with an optical depth below 0.3 are rarely detected by MISR (Marchand et al. 2007, 2010, Mitra et al. 2021) and are not included in the WCTH statistic. Likewise, where optically thin upper level clouds (optical depths greater than 0.3 but less than about 1 to 2) overlap lower level clouds, the MISR stereo-retrieval will often retrieve the CTH of the lower cloud rather than the upper cloud. While not shown in this manuscript, we find that the optically thin high clouds that are detected by MISR have a similar trend in WCTH to that for optically thicker clouds. This suggests the tendency to detect low-level cloud top in this multilayer situation is not likely to affect the trend analysis. Even for optically thick high cloud, the MISR cloud top is not located at cloud top as is typically estimated from spaceborne lidar, as has been recently quantified by Mitra et al. (2021). Rather it tends to be located near the altitude where the cloud optical depth reaches one. This mean penetration depth (for high altitude ice clouds) is comparable or larger than the predicted change in WCTH (which is given in the next section). Any constant offset in CTH is not important to the trend analysis, but in principle, changes in the vertical shape of cloud condensate profiles (within a given optical depth category) could act to change the mean penetration depth up or down and thereby affect the MISR and MISR simulated WCTH trends. The MISR simulator does extract from the model the altitude where optical depth equals one (Hillman et al. 2017), and nominally would capture changes in penetration depth to the degree this is predicted by the model.

2.2 Variability of WCTH in Models and Observations

Determining the time of emergence (TOE) means finding the time at which a true change (in the present case an increase in CTH) can be differentiated with confidence from apparent changes that might arise from random fluctuations due to internal variability, measurement error, or sampling. Thus, to estimate TOE for the MISR observations based on model simulations, we

want the model simulations to realistically represent both the climate trend change (the signal) and the variability (the noise).

The top row of **Figure 1** shows the zonal mean standard deviation of WCTH for both models and the MISR observations. Here the results have been calculated using a 4° grid and are based on monthly data over the period April 2000 to 2015, which are the years that overlap the portion of the model simulation forced with historical emissions and the observational record. The data is deseasonalized by subtracting the mean seasonal cycle before the standard deviation is calculated. Overall, the observations have larger variability in WCTH over most of the subtropics and midlatitudes than both models. However, in the tropics (between -20° and 20°) CESM2 appears to have greater variability than the observations, while IPSL has slightly less variability.

We note that the MISR simulator acts as if it sees the entire globe at once, while in reality MISR can only see a narrow swath below the satellite at any given time. MISR completes roughly 15 orbits each day, sampling a different set of longitudes in each orbit. Even if each day constitutes only three to four independent samples, over the course of the month this would be equivalent to having 100 or more independent samples. To a good approximation (see supplementary material) the increase in the standard deviation in the monthly WCTH measured by MISR due to sampling is given by $\sigma_{internal}/\sqrt{2 * n_{eff} - 2}$, where $\sigma_{internal}$ is the standard deviation of the internal variability in WCTH and n_{eff} is the effective number of independent samples collected by MISR. This suggests the increase in observed variability resulting from the MISR sampling would be less than 10%. The differences in the top panel of **Figure 1** are much greater than 10% (at most latitudes) and we conclude that the differences in WCTH standard deviation seen in **Figure 1** are likely a result of differences in internal variability (between models and between the models and reality) and not a sampling effect.

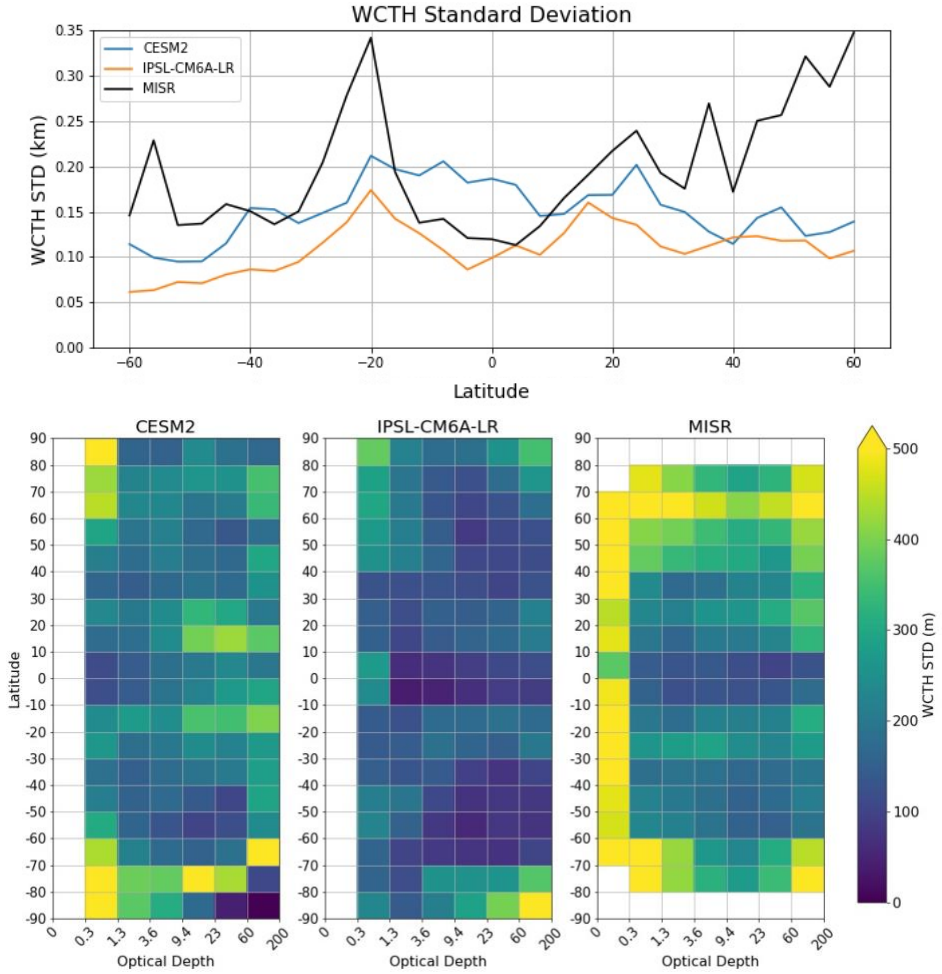

Figure 1 *Top row: Standard deviation of zonal mean WCTH over all optical depth on a 4-degree grid. Bottom row: Standard deviation of zonal mean WCTH on a 10-degree grid separated by optical depth. White cells indicate locations and optical depths where MISR or the MISR-COSP simulator do not have cloud-top-height retrievals. MISR and MISR-COSP data are restricted to the time period from April 2000 to 2015, and are deseasonalized before the standard deviation is calculated.*

In later analysis the data is separated into the different MISR optical depth ranges. The standard deviation of WCTH separated by latitude and optical depth is shown in the bottom row of **Figure 1** for the models and observations (again calculated for the historical period). The latitudinal variability seen in the top panel in **Figure 1** is also clear in the bottom plots as well, but with the additional detail of seeing how variability changes with optical depth. In the MISR observations the high variability in the northern hemisphere poleward of 40° occurs at all optical depths, however there is relatively lower variability between 9.4 and 23, which is the most heavily occupied optical depth category in this region. The magnitude of the variance is much lower in the SH poleward of 40° (compared to NH), but with the optical depth dependence (lowest variability between 9.4 and 23) being the same.

We note that at all latitudes the variability of WCTH in the lowest optical depth range (OD < 0.3) is very large in the MISR observations and these data are not trustworthy. MISR does not typically or consistently detect clouds with optical depths less than 0.3 (Hillman et al., 2017;

Marchand et al., 2010), and the MISR simulator assumes that all high clouds with optical depth less than 0.3 will not be detected (Marchand and Ackerman 2010). Consequently, clouds with an optical depth below 0.3 are not used in the subsequent analysis. There is also substantially higher variance in the MISR observations at latitudes poleward of ±60° that is related to low solar zenith angles and a lack of direct sunlight in the winter months, and we restrict the analysis to latitudes equatorward of ±60°.

Surrounding the equator (-10° to 10°) there are fairly small differences in the MISR observed variability at different optical depths. Both models show greater dependence on optical depth along the equator (-10° to 10°). CESM2 has larger variability (than observations) at optical depths greater than 3.6 and IPSL has lower variability (than observations) for optical depths between 1.3 and 23. In the subtropics (20° to 40° in both hemispheres) there is generally greater variability than in the tropics at virtually all optical depths for the MISR observations as well as the models. CESM2 shows a much higher variability for cloud with optical depth greater than 9.4, which is not seen in the observations or IPSL. Generally, IPSL shows less variability than the observations for optical depths greater than 1.3 at all latitudes. As noted in the top row of **Figure 1** the models produce much less variability in the northern hemisphere midlatitudes and the southern hemisphere subtropics than is seen in observations.

2.3 Calculating Time of Emergence (TOE)

The WCTH metric is used to determine when MISR would be able to detect a change in CTH with a high degree of confidence, if high cloud CTH increases as predicted by the climate models. Timeseries of WCTH are constructed for various latitude bands by first taking the equal-area average of the histogram counts over the region in question in each month (equal-area meaning the histogram in each fixed latitude-by-longitude grid-cell is weighted by the cosine of latitude and includes only grid-cells over ocean). WCTH is then calculated from each monthly histogram using the approach described in Section 2.1. The MISR histogram provides cloud occurrence such that the sum of the component values gives the total cloud fraction, and therefore summing the histograms over the target region yields a WCTH that is weighted by the high cloud occurrence in the model grid cells (latitude, longitude bins).

The seasonal cycle is removed from the WCTH timeseries by subtracting the mean value at each month of the year (averaged over every year along the timeseries starting from April of 2000 to the end of the year 2045) from the initial WCTH timeseries. Then the total mean over all months is added back to restore the timeseries to the correct mean state. After which, the time of emergence (TOE) is obtained as the point in time when a pair of statistics, the slope and Δmean (described below and shown in **Figure 2**), are both nonzero to 95% confidence and remain nonzero for the remaining duration of the timeseries.

The slope statistic is defined as the slope of a least-squares linear regression line. The Δmean statistic is defined as the difference between the mean value calculated over the second half of the time series minus that averaged over the first half of the timeseries. Each statistic is calculated at each year along the WCTH timeseries. This is done starting at the year 2010 and ending at the year 2045, which is well past the TOE for every region and model simulation. So, for every year, both statistics are calculated from the timeseries starting in April of 2000 (the start of MISR retrievals) and ending on the year in question. The process of calculating the statistics along each year of the timeseries is illustrated in **Figure 2**.

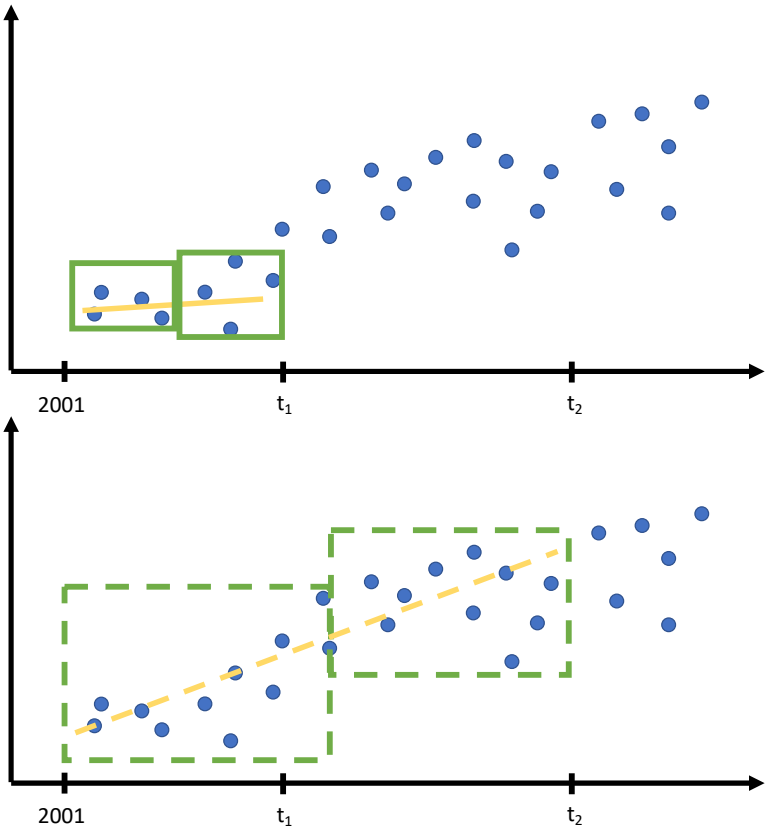

Figure 2 *A diagram of how the two statistics are calculated for each year of the simulation. The top panel shows how the statistics are calculated for some year t_1 then the bottom panel shows the same for some later time t_2. In both, the Δmean statistic is the difference between the mean values encompassed by the green rectangles, and the slope statistic is the slope of the yellow line.*

At each year 95% confidence intervals are calculated for each statistic using a moving-blocks bootstrap technique, which is a resampling scheme that is designed to be used with autocorrelated data. By resampling over a specific sized block of data, the effect of any autocorrelation on time scales shorter than the block length is included in the confidence interval calculation. A detailed description of the method is given by Wilks (1997). An examination of the autocorrelation of the WCTH timeseries is provided in the supplementary materials. Based on this examination, a block length of 24 months was selected as it captures well over 75% of the correlation. The resampling is performed (with replacement) 5000 times, and then the 1-tailed 95% confidence limit is calculated from the resampled distribution.

This analysis is conservative in that for TOE to be designated, both the Δmean and slope statistics are required to remain nonzero to 95% confidence for the remainder of the model simulation. Of course, in application one doesn't know the future so the "remainder" isn't known. However, we find it to be rare for both of our metrics to be triggered with significance and even one test statistic to lose significance later in the simulation. When that did occur, the loss-of-significance was delayed by no more than 2 years.

2.4 Scaling of Model CTH Variability to Match Observations

It was found in Section 2.2 that in many regions there is greater variability in the observational record than is produced in the models running the MISR simulator. It is essential to represent the variability that MISR observes accurately to calculate a realistic time of emergence for a trend in WCTH. Consequently, we increase the variance in the simulated time series as follows, in which the time series of WCTH is treated as the sum of a forced and random term:

$$WCTH^{MISR}(t,\varphi) = WCTH^{true}_{forced}(t,\varphi) + \partial WCTH^{MISR}_{var}(t,\varphi) \quad (2a)$$

and

$$WCTH^{model}(t,\varphi) = WCTH^{model}_{forced}(t,\varphi) + \partial WCTH^{model}_{var}(t,\varphi) \quad (2b)$$

where $\partial WCTH_{var}$ is a random variable representing the variability of the WCTH, and $WCTH_{forced}$ is the forced response at some time and taken over some set of model grid-cells denoted by φ. Ideally $\partial WCTH^{MISR}(t,\varphi)$ would be well represented by $\partial WCTH^{model}(t,\varphi)$, however this was not found to be the case in Section 2.2 where the variability in the models was found not to match well with the observations during the historical period (2001-2015). Thus, a linear approach is taken to matching the observed and simulated variabilities.

$$WCTH^{model}(t,\varphi) = WCTH^{model}_{forced}(t,\varphi) + R(\varphi) * \partial WCTH^{model}_{var}(t,\varphi) \quad (3a)$$

where

$$std[\partial WCTH^{MISR}_{var}(t,\varphi)] = R(\varphi) * \ std[\partial WCTH^{model}_{var}(t,\varphi)] \quad (3b)$$

$std[-]$ denotes taking the standard deviation of the timeseries, $R(\varphi)$ is a constant (in time) that we refer to as the *scaling factor*. We determine the scaling factor by finding the ratio of the observed and modelled variability during the historical period. More specifically, the scaling factor is calculated by first removing any linear trend from the WCTH time series for both the observations and the model simulations. After this trend removal, the standard deviation is calculated from each times series, and $R(\varphi)$ is calculated as the ratio of the observed standard deviation to the modeled standard deviation using only the historical period. To produce a conservative estimate for TOE, the regions where the variability is greater in the models than the observations are left unchanged. That is, we calculate $R(\varphi)$ as:

$$R(\varphi) = \ std[\partial WCTH^{MISR}_{var}(t_{obs},\varphi)] \ / std[\ \partial WCTH^{model}_{var}(t_{obs},\varphi)] \quad (4a)$$

$$if\ R(\varphi) < \ 1, then\ R(\varphi) = 1 \quad (4b)$$

Where t_{obs} spans from April 2000 to 2015.

It is important to note that this method does allow for the variability to change in time. The standard deviation is not forced to match the observed standard deviation for the entire run; rather the standard deviation of the entire run is scaled up by a constant factor so that the standard deviation matches observations during the historical period, and the variability after 2015 can be different from the historical period. After this technique is applied to the data, the time of emergence analysis, as described in Section 2.3, is performed on the WCTH time series to determine TOE.

On a minor note, we also examined an additive model for increasing the variability:

$$std[\partial WCTH_{var}^{MISR}(t,\varphi)] = std[\partial WCTH_{var}^{model}(t,\varphi)] + C(\varphi) \quad (5)$$

Where $C(\varphi)$ is a constant *additive factor*. The scaling and additive methods result in nearly identical TOE, and so only the multiplicative scaling is presented here. But a detailed description of the additive approach is available in the thesis that accompanies this work (Aerenson, 2021).

3. Time of Emergence (TOE) Results for CESM2 and IPSL-CM6A-LR

The methods described in Section 2 were applied to outputs from CESM2 and IPSL SSP5-8.5 simulations to predict when MISR should be capable of detecting a trend in cloud-top-height. The trend analysis is carried out over various regions and latitude bands, both with and without the variance adjustment described in Section 2.4. In **Figure 3** the timeseries of WCTH is shown for the Northern midlatitudes, as well as the timeseries of the Δmean and slope statistics, with their 95% confidence intervals. The left and right columns show the results without and with the variance scaling respectively. The top panels show the observed and model WCTH time series. Comparing the model WCTH time series between the top left and right panels (orange and blue lines) shows how variance scaling has substantially increased the variability in the model WCTH time series. Also, the observed WCTH (black line) is greater than the WCTH calculated from the models, with the observed WCTH being above 8 km while the model WCTH are generally below 8 km. The models have a variety of biases with respect to the observations, including the WCTH. We provide a brief examination of model biases in the supplementary material (Text S1, Figures S1 and S2), and will discuss the topic further in the concluding section.

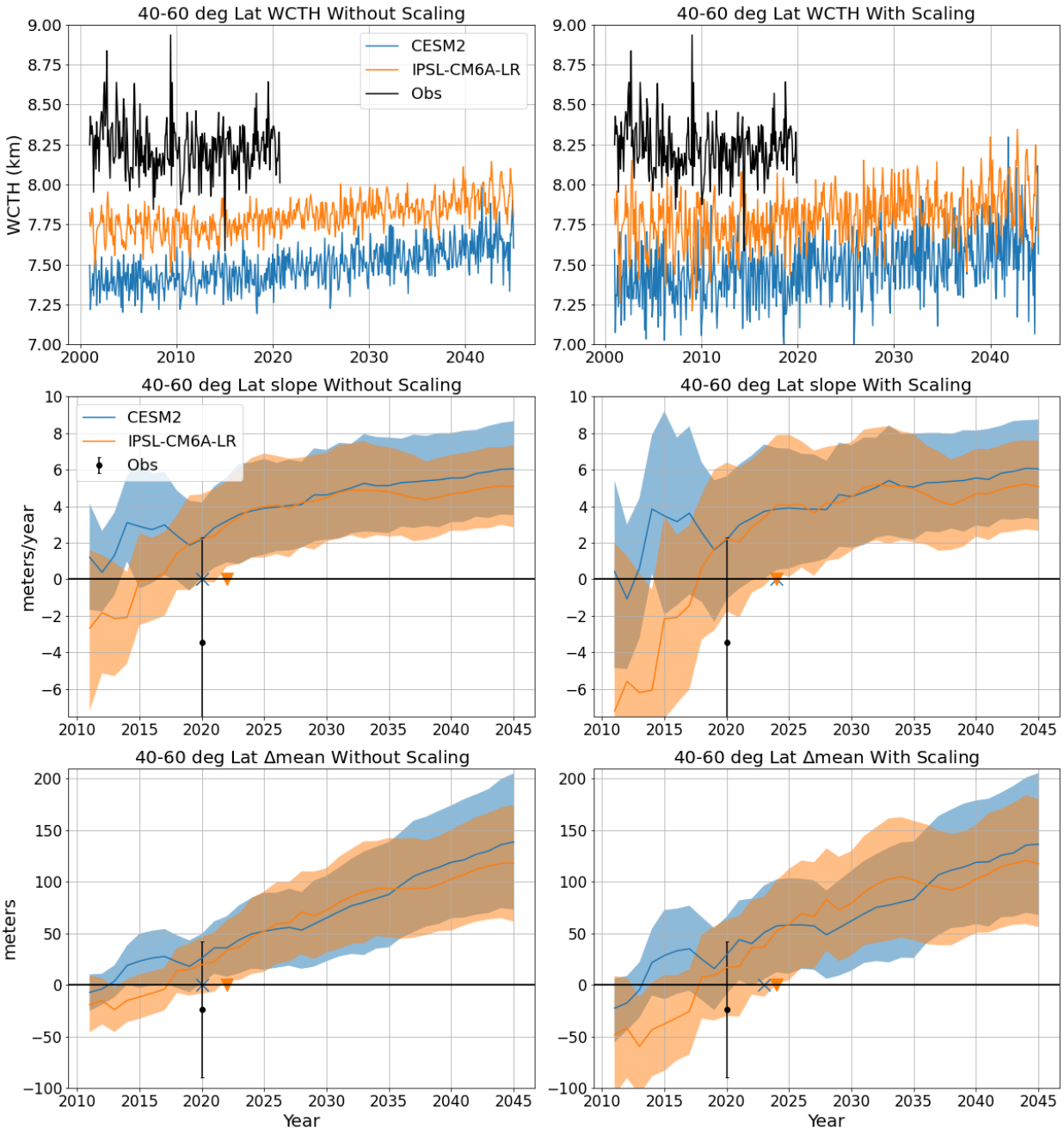

Figure 3 *Upper left: deseasonalized WCTH timeseries for the MISR observational record and both models, calculated with all cloud with OD > 0.3, averaged over the NH midlatitude oceans. Upper right: Same as upper left, but with the variance scaling applied. Middle left: slope statistic and confidence intervals calculated at each year starting in 2010 for each model, shown in black is the statistic calculated for the full observational record. Middle right: same as middle left, but with the variance scaling applied. Bottom row: The Δmean statistics are shown with and without the variance scaling applied.*

The lower two rows of plots show the two statistics used to determine TOE. Here the colored lines are the slope (middle panels) and Δmean statistic (bottom panels) calculated for the time series made from the time of the earliest of MISR observation (April 2000) and ending in

each year from 2010 to 2045. The shading indicates the 95% confidence limits, which were found using the moving block bootstrap technique, described in Section 2.3. As one expects, the shaded region in the right panels is wider, because of the scaled-up variability. The TOE is defined as the time when the confidence intervals of both statistics exceed zero, and remain above zero until the end of the simulation. The TOE date for each statistic is marked by an X or a triangle for CESM2 and IPSL respectively. The black dot and bars show the statistics and 95% confidence intervals for the current MISR observational record, ending in June of 2020.

The overall TOE is determined by finding the point at which both statistics are significant. When the variance scaling is not applied to the analysis, TOE occurs at 2020 in CESM2, and at 2022 in IPSL, and the TOE is delayed by the variance scaling, so that when the variability is forced to match the observations, both models predict TOE at 2024.

The timeseries of WCTH (calculated as described in Section 2.3) for four additional latitude bands and "globally" for all oceans between -60° and 60° latitude are shown in **Figure 4**, with slope and Δmean statistics in **Figure 5**. The "global" average is found by averaging results for the 5 zonal latitude bands, each weighted by the area covered by ocean in each latitude range. Here only results with variance scaling are shown.

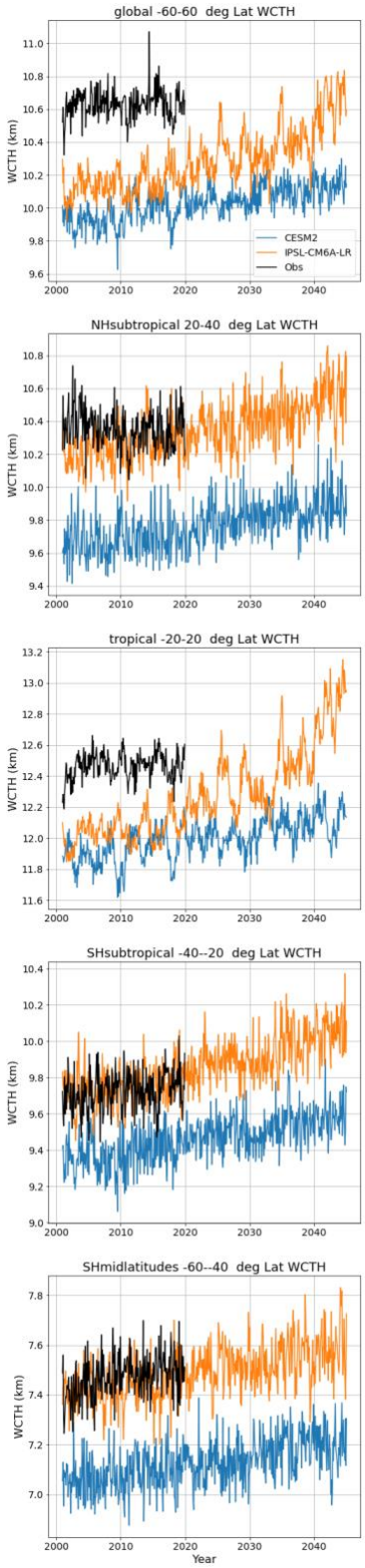

Figure 4 *Deseasonalized timeseries of WCTH, calculated with all cloud with OD > 0.3, averaged over tropics, subtropics and midlatitudes, as well as global mean. The observations are shown alongside the model output with the variance scaling applied.*

In the tropics (third panel of **Figure 4**) both models display variations in WCTH that are correlated on longer scales than at other latitudes. This is due to the El Niño Southern Oscillation (ENSO). Both models initially begin with a similar upward trend in WCTH, but after 2035 the WCTH in IPSL increases more rapidly than CESM2 in the tropics. We discuss this large change further in Section 4, but as we will see momentarily it is not important for the estimated TOE, as the increase in CTH becomes detectable in both models before 2025. Overall, the two models behave much more similarly to each other in the subtropics and midlatitudes than in the tropics.

Figure 5 shows how the slope and Δmean statistics change during the simulation and their accompanying 95% confidence intervals. As with **Figure 4**, the results shown in **Figure 5** do have the variance scaling applied. The results of the TOE calculation, with and without variance scaling, are given in **Table 2**. Overall, **Figure 5** shows a similar pattern of WCTH increase in each model simulation, despite the climatological (base state) differences between the models. The rate of WCTH increase is typically slightly greater for IPSL than it is for CESM2, but the difference is small, and is well within the 95% confidence intervals for all regions. Both models predict that MISR should be capable of observing a trend in CTH in all latitude bands by 2024, and in the global mean before 2023. For the most part the models are in agreement within a 2-year range. The variance scaling does matter, and delays the detection as much as 4 years, depending on the model and the latitude band, and is most significant in the Northern Hemisphere, where variability of observed WCTH is larger than that simulated by the models.

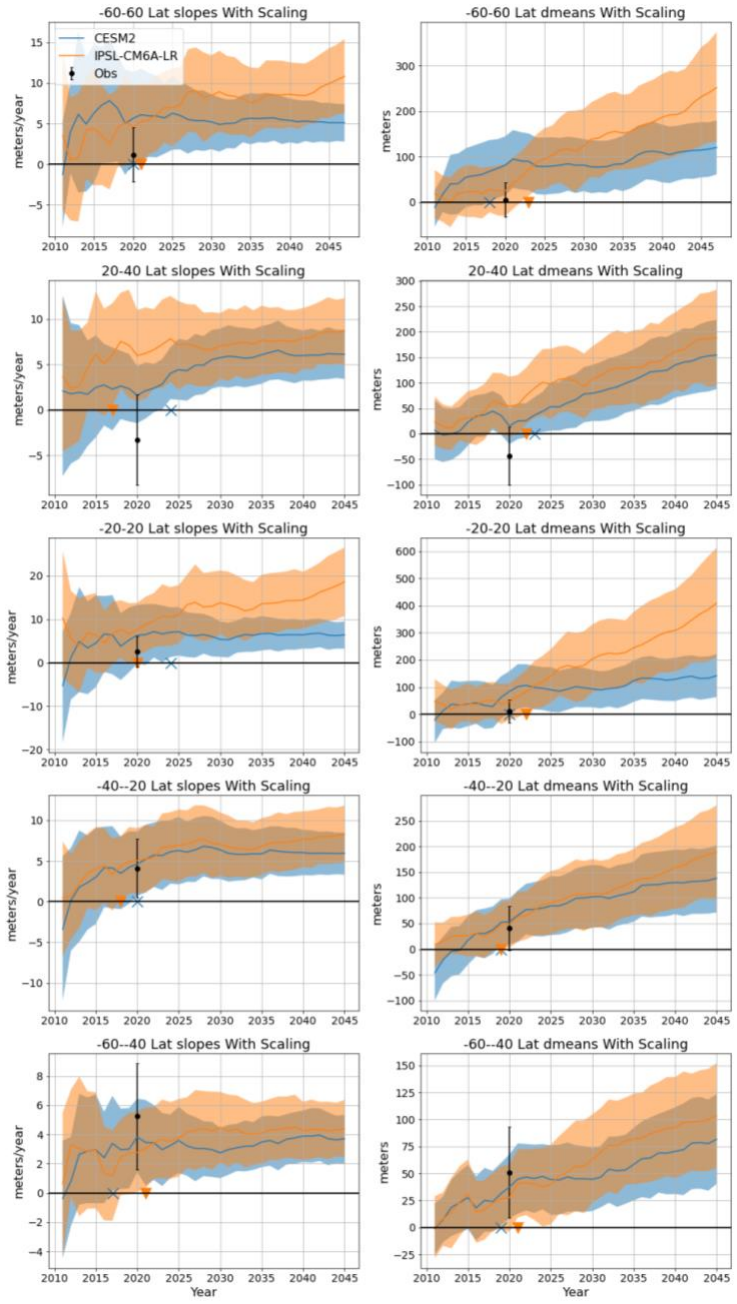

Figure 5 *Plots of the same format as the bottom two rows of* ***Figure 2*** *but shown over the other remaining regions. Right column is the slope statistic at each latitude range, left column is the Δmean statistic. The plots shown do include the variance scaling.*

With variance scaling, TOE is earlier in the SH than the NH, and the model results suggest that MISR observations (which currently extend through June of 2020) should have detected, or be close to detecting a change in the SH. Indeed, the observation results in **Figure 5** (the black dot and bar) show that MISR has observed an increase in CTH that slightly or nearly exceed the 95% confidence for a non-zero change in the SH, suggesting that there has been a statistically significant increase in CTH. However, analysis by Geiss & Marchand (2019) suggest that MISR changes in SH may be an El Niño Southern Oscillation (ENSO) signal rather than a

broad increase in CTH. In the global mean, the CESM2 simulation also suggests that MISR should have detected (or be very close to detecting) a global trend, which it has not. This will be discussed further in the concluding section.

	CESM2		IPSL-CM6A-LR	
Variance Method	Model's Innate Variance	With Variance Scaling	Model's Innate Variance	With Variance Scaling
Global	2020	2020	2021	2023
NH midlatitudes	2020	2024	2022	2024
NH subtropics	2022	2024	2018	2022
Tropics	2022	2022	2022	2022
SH subtropics	2020	2020	2018	2019
SH midlatitudes	2019	2019	2018	2021

Table 2 *TOE as calculated from each model at 5 different latitude bands. TOE calculations were performed with and without the variance scaling described in Section 2.4*

To this point all analysis has been performed on the full optical depth range that is confidently detected by MISR (greater than 0.3). We would like to understand if there are preferential optical depths and narrower latitudes where early trend emergence may occur. In **Figure 6,** the same TOE analysis is performed on WCTH calculated on smaller latitude ranges and at specific optical depths to understand the zonal and optical depth structure of the TOE. Variance scaling is applied, with scale factors calculated for each latitude and optical depth range. Narrowing the analysis to smaller latitude and optical depth ranges largely produces later TOE than the broad ranges shown in **Table 2**. The few latitudes and optical depth ranges where TOE is earlier than those given in **Table 2** are marked with white text. There is only 1 such range for CESM2, and only 4 for IPSL. With 84 total latitude and optical depth bins occupied, and a 95% confidence threshold, one expects by random chance that a few bins would result in an early TOE (and these few earlier detections would not pass a field significance test). In general, the CESM2 and IPSL models produce very different structure of TOE in latitude and optical depth and there is no clear pattern in optical depth that results in earlier detection. While not presented here, in the accompanying thesis work (Aerenson, 2021) we did examine other approaches to improve TOE by preferentially selecting longitudinal regions or optical depth ranges with relatively low observational variance and found this had little or no benefit relative to using full (over ocean) averages of fairly wide (at least 20°) latitudinal bands. And while MISR observations have not been processed over land (owing to difficulties in the retrieval optical depth over land), we found little advantage to focusing on CTH over land in the models, except in the NH midlatitudes where TOE was improved by 2 or 4 years, in CESM2 and IPSL respectively. Based on these limited data, we conclude that the most effective way to detect trends in CTH is through broadly averaged zonal means.

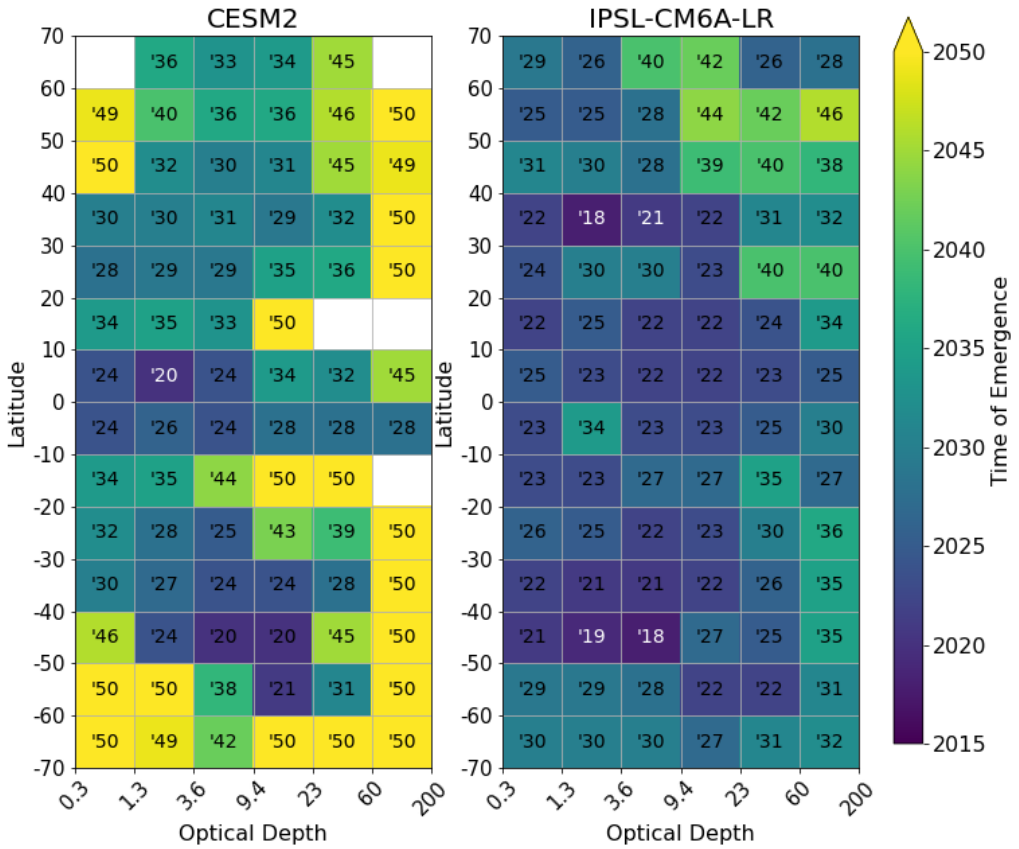

Figure 6 *Time of Emergence calculation is performed on zonal mean WCTH calculated on a 10-degree grid, for each individual optical depth bin with the variance scaling applied. Results of such calculations are shown as the pixel coloring and the overlaid numbering. The numbers all represent years in the 21st century., white pixels show regions where there is insufficient cloud to perform the TOE calculation which is defined as more than one tenth of the months having no cloud in that given category. White numbers indicate pixels corresponding to TOE earlier than the broad zonal mean value given in* ***Table 2.***

4. Consistency of Rising WCTH with the FAT Hypothesis

As described in the background material, the FAT hypothesis asserts that the CTH of high clouds will remain at a nearly fixed temperature. This section asks whether the change in CTH seen in the models is consistent with this hypothesis.

To do this, the WCTH calculated from the model output is compared with two forms of synthetic WCTH that are calculated assuming a perfect FAT response in CTH, as well as in a perfect Fixed-Anvil-Pressure (FAP) response. The FAP response can be viewed as the climate response where anvils do not rise in the atmosphere, such that in the FAP response the anvil cloud would remain at the same pressure, and warm at the same rate as the surrounding atmosphere. The synthetic WCTH that follows a perfect FAT response is calculated by first averaging the temperature profile in the cloudy part of each region. This is done by calculating the cloud-fraction-weighted average of the temperature profile over the region of interest:

$$T(z_{model}, t) = \frac{\sum_{lat,lon}(ta(z_{model}, lat, lon, t) \times \sum_{z>thresh} CF_z(lat, lon, t))}{\sum_{z>thresh,lat,lon}(CF_z(lat, lon, t))} \quad (6)$$

where ta is the model's temperature profile on its native height grid, where z_{model} represents a level on that model's height grid, CF_z is the MISR high cloud fraction at each grid level (found by summing MISR CTH-OD histogram components at all optical depths), averaged over the observational period 2001-2015, the subscript $[-]_z$ represents the discrete heights of the MISR CTH-OD histogram, and $T(z_{model}, t)$ is the resulting average temperature profile of the cloudy-sky portion of the region of interest. This profile is then interpolated to match the vertical spacing of the MISR CTH retrievals, so $T(z_{model}, t)$ is averaged over the observational period and linearly interpolated on to the MISR vertical grid denoted below as T_z, and this is used to calculate the weighted cloud-top-temperature (WCTT) for the MISR profiles in a similar way to the WCTH for the observational period as:

$$WCTT(t) = \frac{\sum_{z>thresh}(T_z(t) \times CF_z(t))}{\sum_{z>thresh}(CF_z(t))} \quad (7)$$

Finally, the FAT WCTH is calculated by assuming WCTT remains constant over time. Specifically, the FAT WCTH is taken as the altitude where $T(z_{model,}, t)$ matches WCTT from the historical period, found via linear interpolation between the levels of $T(z_{model,}, t)$. We stress the FAT WCTH is calculated from the historical cloud profile, and simulated future temperature profiles, and this method does not account for any possible changes in cloud vertical profiles caused by warming (other than shifting upwards), which might occur because of changes in global circulation patterns or local dynamical or thermodynamic effects including those related to stability consideration. We introduce this metric only to contextualize the simulated WCTH results from fully coupled CESM2 and IPSL simulations.

The FAP WCTH is calculated using the same method as the FAT WCTH, except the pressure profile rather than the temperature profile is used, so that FAP WCTH is equivalent to assuming clouds remain at a constant pressure with warming.

The results of the FAT and FAP calculations are shown in **Figure 7** along with the WCTH calculated directly from the MISR simulator output for the CESM2 and IPSL models which ran the SSP5-8.5 scenario with the MISR simulator. The results are shown for the tropics (top panels) and Northern Hemisphere subtropics (middle panels) and midlatitudes (bottom two panels). Results for the Southern Hemisphere are not shown, but are characteristically similar. A confirmation of the FAT hypothesis would appear as the directly simulated WCTH (blue/orange lines) increasing at the same rate as the WCTH calculated with a fixed temperature profile (green line, labeled FAT). In the subtropics and midlatitudes, the WCTH of both CESM2 and IPSL WCTH increases slightly slower than FAT, but faster than the FAP WCTH, and is consistent with the behavior predicted by the PHAT hypothesis that the rate of rising anvils will be suppressed by increasing static stability in the upper troposphere (Zelinka & Hartmann, 2010).

The situation is more complicated in the tropics of the IPSL model. In IPSL, the WCTH increases at a rate faster than is suggested by FAT. More specifically, the increase in WCTH is much faster between 2030 and 2050, but then slows down at 2050 such that by the end of the century WCTH has increased by the same amount as the FAT projection. This response is examined in detail in the supplementary materials (**Text S3 and Figure S5**) as well as the accompanying thesis (Aerenson, 2021), and is an artifact of the MISR discretization that arises

when the vertical distribution of high clouds occurrence is narrow compared with the size of the discrete MISR CTH categories (which is 2 km in the upper troposphere). The artifact does not appear in the CESM2 results because the vertical distribution of high clouds is wider than in IPSL, and compares better with the observed distribution.

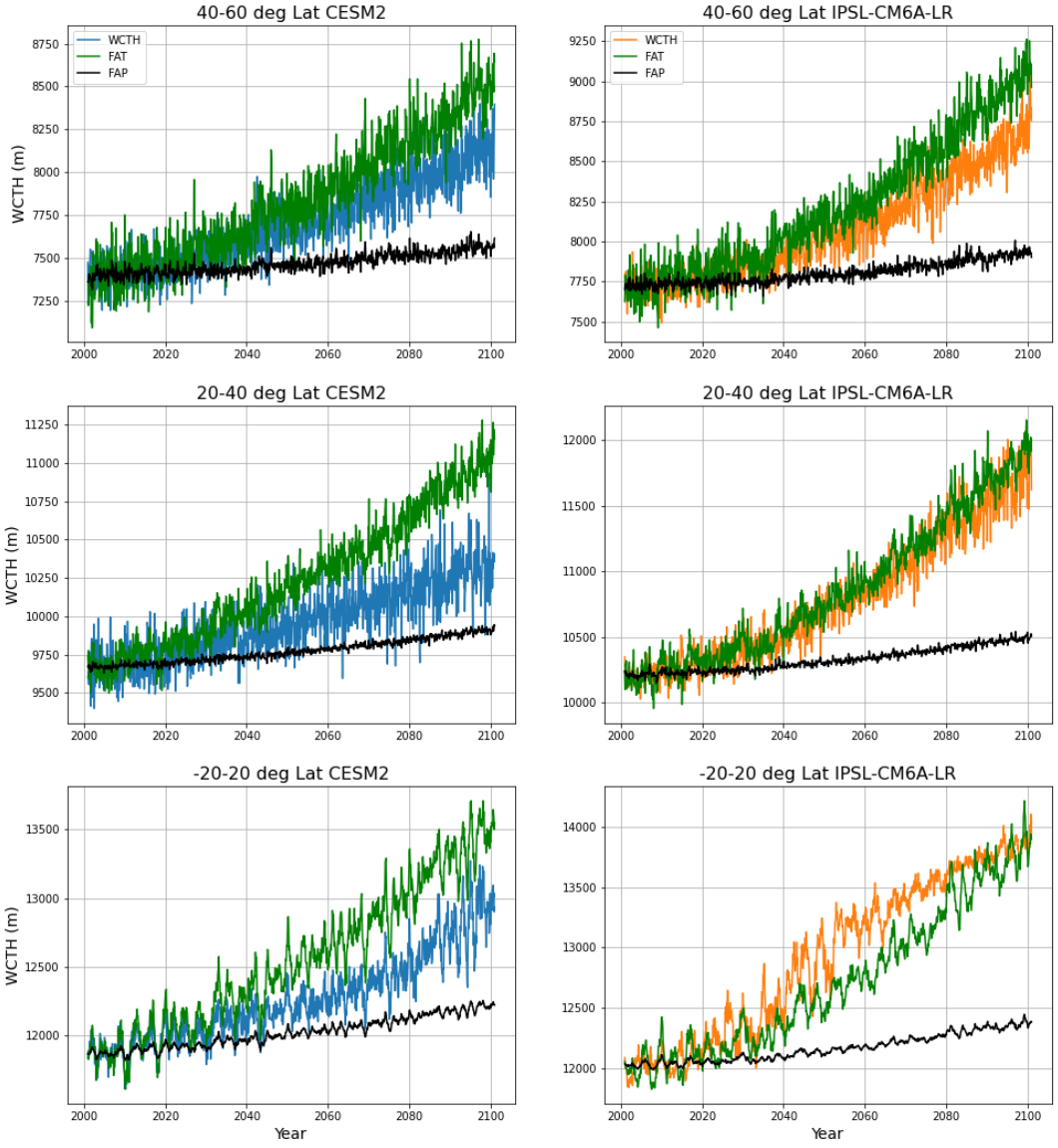

Figure 7 *WCTH is shown for each model alongside the synthetic WCTH that is calculated assuming a perfectly FAT condition and FAP condition. Timeseries are shown for the tropics and both Northern Hemisphere regions, and are extended to include the entire 21st century. The seasonal cycle is removed via a 25-year running average so that any change in the seasonal cycle (which can occur when viewing the full 100 year simulation as opposed to the previous figures only concerned with the first 45 years) does not impact the timeseries shown.*

In spite of the discretization problems, the increase in CTH based on the assumption that the FAT hypothesis appears to be a reasonably good approximation, at least for the period up to 2040, though we expect the FAT assumption will result in a somewhat earlier than true TOE. We

exploit this in the next section to extrapolate or create synthetic WCTH timeseries for several additional models that ran the MISR simulator during AMIP simulations, but did not run the MISR simulator during their SSP5-8.5 simulations in order to gauge the spread in TOE one might expect from a larger set of models.

5. Synthesized WCTH Forecast Using AMIP runs and the FAT Hypothesis

As discussed in Section 2.2, the detection of change in CTH can be viewed as a signal to noise problem. In the analysis presented in Section 3, the signal was based on output from two models, CESM2 and IPSL-CM6A-LR, which ran the MISR simulator as part of their SSP5-8.5 simulations. However, both IPSL-CM6A-LR and CESM2 warm quickly relative to other climate models and have above-average Equilibrium Climate Sensitivity (ECS): CESM2 has an ECS of 5.2 K per doubling CO_2 and IPSL-CM6A-LR has an ECS of 4.6 K per doubling CO_2 (Meehl et al., 2020). One presumes the TOE would occur later if warming occurs more slowly, and in general there is likely to be some variability (spread) in the rate of CTH increase between models per degree of increase in surface temperature. To investigate these possibilities, we synthesize WCTH timeseries for models that (1) produced MISR simulator output for the AMIP run and (2) ran the SSP5-8.5 simulation (regardless of whether or not the MISR simulator output was produced) under the assumption that high cloud CTH will rise with a fixed temperature distribution. As shown in Section 4 the change in MISR simulated WCTH in the CESM2 and IPSL-CM6A-LR is reasonably well approximated by a FAT-like increase in CTH (at least out to 2040). In addition to CESM2 and IPSL-CM6A-LR, the models examined in this section are MRI-ESM2-0, CanESM5, CNRM-CM6-1, CNRM-ESM2-1, and BCC-CSM2-MR. The synthetic WCTH time series are created following the approach described in Section 4, except instead of calculating the WCTT based on the historical period (as was described in Section 4), the WCTT is calculated using the AMIP run from 2001 to 2015. Then the temperature profile from the historical and SSP5-8.5 fully coupled model simulations are used to calculate the height at which the AMIP WCTT occurs in the historical and SSP5-8.5 simulations from 2001 to 2100; and the same TOE analysis used in Section 3 is applied to the AMIP synthetic WCTH projections (including the scaling of the variability to match the MISR observed WCTH variability).

In **Figure 8**, the left panels show the average rate of increase of each AMIP WCTH projection from 2001 to 2045, and the right panels show the estimated TOE (based on both the slope and Δmean statistics showing positive change in CTH with 95% confidence). The rate of increase and TOE are plotted against the ECS (top panels), Transient Climate Response (TCR, middle panels), and global mean surface temperature anomaly (bottom panel, calculated as the difference between the 2035-2050 average and the 2001-2015 average) for each model. The average ECS and TCR from the full CMIP6 ensemble is 3.7 K and 2.0 K, with standard deviations of 1.1 K and 0.4 K respectively (Meehl et al., 2020). Data from all five latitude bands are plotted together and denoted by the different symbols (legend shown in top left panel), and each model corresponds to a different symbol color with the model name and values labelled along the horizontal axis of each panel.

The results shown in the left panels of **Figure 8** indicate that in almost all seven of the models and by all three metrics, the average rate of increase in CTH (which in this analysis is synonymous with the rate of temperature increase in the upper troposphere) is fastest in the tropics and slowest in the SH midlatitudes. However as noted earlier, the amount of variance in

CTH differs appreciably with latitude and the fast change in the tropics does not always lead to the earliest TOE. In fact, most models show the earliest TOE occurs for the SH midlatitudes with considerable variability regarding which latitude zone will have the latest TOE.

As regards the relationship between warming rate and TOE, the CanESM5 model has the strongest warming by all three metrics and the earliest TOE; while the MRI-ESM2-0 and BCC-CSM2-MR models that have the lowest ECS and TCR values, also have some of the latest TOE. Overall, we can conclude that while there is a clear tendency for the models with faster warming to have larger trends in CTH (left panels), this does not necessarily lead to earlier TOE (right panels), and there does not appear to be a clear relationship between ECS, TCR or global mean surface temperature anomaly with TOE. Nonetheless these results suggest that the TOE estimates presented in Section 3 could occur by as much as 5 years later (roughly 2030), given the model spread.

As a reminder, we stress that the results in **Figure 8** are for the FAT-like increase which is faster than the true change in CTH, and the TOE shown here is expected to be earlier than the true TOE would be (because true CTH is expected to increase more slowly than FAT following the PHAT hypothesis and **Figure 7**) and these results may not capture regional differences accurately (since latitudinal deviations from FAT are possible if not likely). Rather the point of this analysis is only to investigate the spread in TOE values one might get from a larger ensemble of models and to investigate the potential for delay in TOE that we might expect from models that warm more slowly than CESM2 and IPSL.

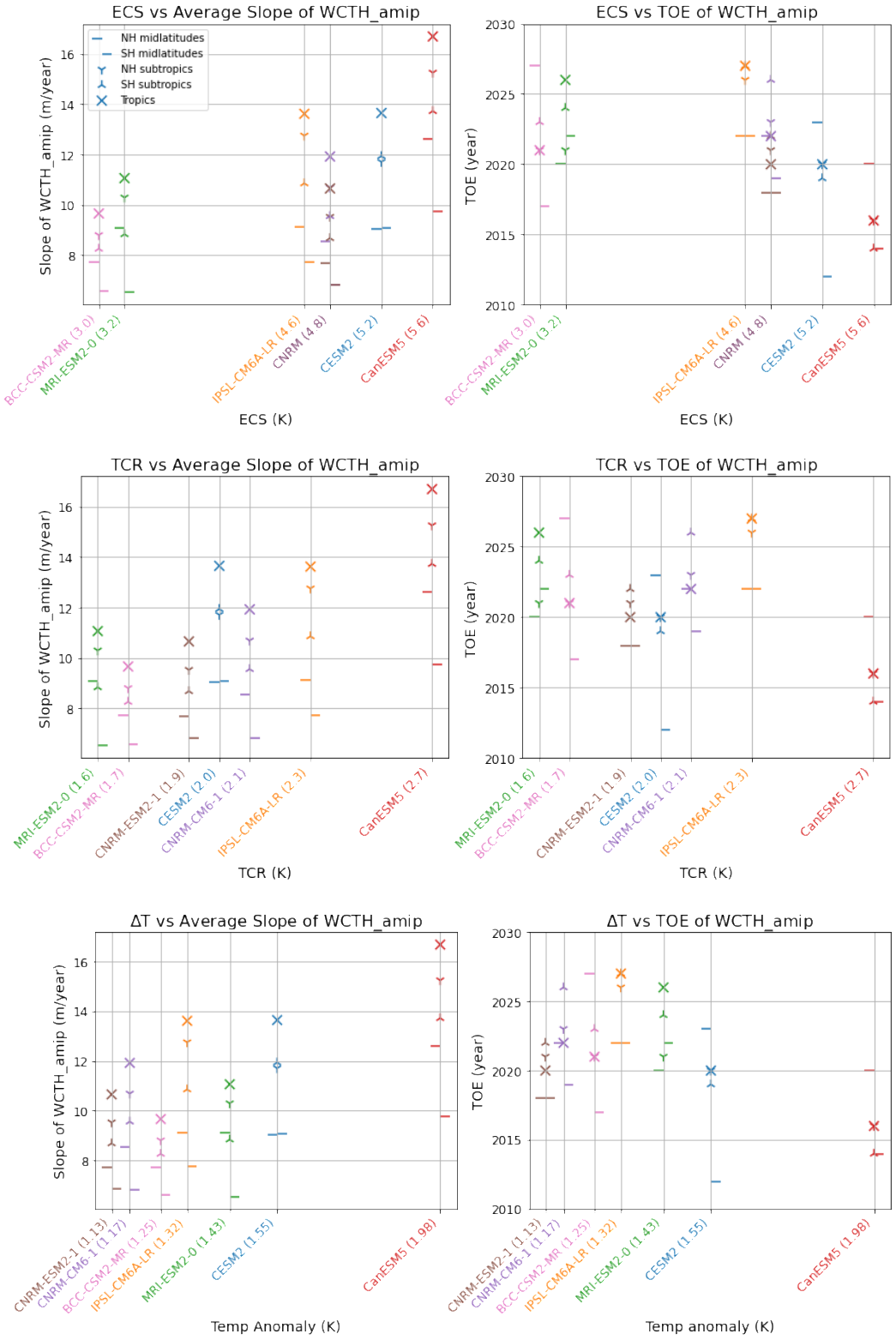

Figure 8 *Rate of change of AMIP WCTH is plotted against the Equilibrium Climate Sensitivity (ECS), Transient Climate Response (TCR), and temperature anomaly in the left panels. All five latitude bands considered are plotted together, but the latitude bands are marked by different*

shapes, and the models are each different colors. The ECS, TCR, and global mean temperature anomaly are in parentheses next to the corresponding model name. The right panels show the results of the TOE calculation plotted against ECS, TCR and Temperature anomaly. In the top row, where ECS corresponds to the horizontal axis, both CNRM-CM6-1 and CNRM-ESM2-1 have the same ECS so it is simply labeled as CNRM.

6. Discussion and Conclusions

In a warming climate, the FAT and related PHAT hypotheses predict that the altitude or height of anvil detrainment and high-altitude clouds will increase following the height of a nearly constant temperature level, which creates a positive climate feedback. Climate models (nearly without exception) predict an increase in high cloud altitude, but the rate of increase varies between models. The satellite record to date provides little evidence of a global increase, which is unsurprising because of the small magnitude of the change relative to internal variability. In this study we use output from several CMIP6 models to determine when measurements by the NASA MISR instrument (which determines cloud-top-height using a stereo-imaging technique) might be expected to detect an upward trend in high cloud altitude over ocean. The model simulations employ a MISR simulator which produces histograms of cloud-top-height and optical depth consistent with those obtained from the MISR instrument, and a scheme was developed to calculate a weighted cloud-top-height (WCTH) metric for high clouds based on the histogram data. This metric, in combination with Δmean and slope statistics, and bootstrap resampling is used to determine a Time of Emergence (TOE) for the detection of change in WCTH with 95% confidence (in both statistics). The models were found to often underestimate variability in the MISR observation over the time period of the current observational record, and the model variability was scaled to match that found in the MISR data over the current observational record in the analysis.

The TOE analysis is performed using two CMIP6 models: CESM2 and IPSL-CM6A-LR, both of which generated MISR simulator output while running the ScenarioMIP SSP5-8.5 experiment. Both models predict that MISR will be capable of observing a trend in CTH sometime in the next 5 years (by 2024) in tropical, subtropical and mid-latitude zonal means of both hemispheres, and the models predict that in the Southern Hemisphere (SH) MISR should already have been capable of detecting trend in CTH. In fact, the MISR observations do show an increase (a positive trend) in the zonal mean WCTH in the SH midlatitudes (40° to 60° S) and a nearly significant change (just below the 95% level of confidence) for the SH subtropics. However, it is not clear that the observed SH trend is due to climate change rather than due to variations with ENSO and the Southern Annular Mode (SAM). Geiss and Marchand (2019) have shown that regional-scale variation in cloud amounts in the MISR CTH-OD histograms in the SH midlatitudes are dominated by variations that are strongly correlated with ENSO and SAM. Arguably, trends need to be confirmed in the Northern Hemisphere to firmly establish a global change in CTH is occurring.

The analysis of global mean WCTH shows that for both models global TOE occurs earlier for the global average than for the NH midlatitudes, and later or the same as the TOE for the SH. It is worth noting that the average is weighted by the ocean area, and this method inherently places greater weight on the Southern Hemisphere than the Northern Hemisphere. For this reason, it is important to be cautious with the interpretation of the global results. CESM2 predicts that MISR should already be capable of detecting a global trend. This may be due to the greater

weight placed on the Southern Hemisphere in the global averaging, but in general, both CESM2 and IPSL simulate a stronger increase in WCTH in the NH than has been observed. For example, in **Figure 3** one can see that the slope statistic for the MISR observations (black dot) does not fall inside the 95% confidence limits given by the models for the change in WCTH in the NH midlatitudes, even when the variance scaling is applied. The same is true in the NH subtropics in **Figure 5** for both the slope and the Δmean statistics. We speculate that CESM2 and IPSL have a rise in CTH in the NH that is too strong – though to be clear there remains considerable uncertainty in the observational estimated trend statistics and further observations are required to confidently reject the possibility that the apparent difference to date is not a result of internal variability.

The earlier detection in the SH is a result of the lower internal variability in the zonal mean WCTH in the SH. If anything, the models suggest that the upward trend in WCTH will be smaller in the SH than the NH (see left panels of **Figure 8**). The MISR observations and this analysis are restricted to ocean, and the lower variability over SH ocean is largely, but not entirely, due to the fact that there is more ocean (and hence more sampling in the zonal mean) in the southern hemisphere. We conducted several experiments where we selected a portion of the SH midlatitudes (40° to 60° S) which was equal in area to the NH midlatitudes. As one might expect this increased variability and delayed the detection time, but the time remained slightly earlier for the SH than the NH. Fundamentally, the increase in CTH is larger (in both models) in the NH but so is variability. IPSL seems to capture the hemispheric asymmetry of WCTH variability reasonably well, in that it has greater WCTH variance in the NH than SH (though we stress that it underestimates variability). CESM2 does not appear to capture the hemispheric differences in the WCTH. In general, the models do not capture well the variability in WCTH observed by MISR, and therefore the model output was scaled to match the observed variability in the TOE analysis.

As noted in the introduction, T19 found that trend detection in CTH measured by CloudSat occurs first in the subtropics or lower-midlatitudes (latitudes between 20^o to 60^o) of both hemispheres, with slightly earlier detection times for northern hemisphere. This differs from the results presented here in that we find the trend detection occurs earlier in the SH than in the NH. As discussed in the preceding paragraph, this is largely due our need to restrict the analysis to oceans, which T19 did not need to do using CloudSat observations (as the radar high cloud detection has little sensitivity to surface conditions). Regarding the detection time, we note that T19 did not apply any variance adjustment in the results presented in their primary manuscript (and rely directly on the model simulated variance). They did this because the relatively short CloudSat data record made it difficult to quantify the observational variance with sufficient accuracy. However, in their supplementary materials (figures S15 and S16) they do present results based on the observed CloudSat variability and find this delayed detection by as much as 5 years, which is broadly consistent with what we find here when relying on the model variance. This suggest that the CloudSat detection times presented by T19 in the main manuscript (and starting in the mid to late 2020's) are probably somewhat optimistic. We note the CloudSat record begins in June of 2006 (6.5 years later than MISR), and overall it appears that CloudSat and MISR require a data record length of about 20 years for CTH trend detection in the SH (between 20° and 60°), in spite of differences in the measurement techniques (based on W-band radar reflectivity vs. optical-stereo). In the NH (at least at mid latitudes), CloudSat would obtain a detection with a similar 20 year record while MISR will take longer (about 25 years) because of the greater amount of land limiting the MISR data, though in principal the MISR observations

could be processed to produce a CTH and OD over (snow-free) land - where one expects that MISR data would be of good quality for clouds with optical depths greater than 3 (where issues related to surface albedo are reduced). In the tropics, on the other hand, detection remains significantly later in the tropics in T19 (with cloud radar) due to higher internal variability in radar reflectivity profiles. C18, on the other hand, suggest that a CALIPSO-like lidar record would need to be 25-26 years long in the tropics, and 29 years long in the Southern Ocean to detect a trend to 90% confidence. While there are differences in TOE detection techniques and the climate models used (between C18 and this study), as well as SST pattern differences (between AMIP and coupled runs), we speculate that the longer detection times in C18 are primarily a result of their analysis assumptions. Specifically, the C14 and C18 analysis is based on a linear interpolation between AMIP and AMIP +4K simulations, and it is assumed that a 4 K temperature increase would take ~100 years. The SSP5-8.5 simulation used here has substantially more warming than 4 K for nearly all models, with most models having more than 6 K of warming and some reaching as much as 7 K of warming by the end of the century (Tebaldi et al., 2020).

The differences between our results using the SSP5-8.5 simulation and the C14 and C18 analysis highlight the importance of emissions and warming pathways when forecasting climate trends. SSP5-8.5 is the highest warming emission pathway of the suite of simulations designed for CMIP6 (O'Neill et al., 2016). Hence, one expects that if there is sufficient mitigation policy MISR TOE could be delayed. In general, CESM2 and IPSL-CM6A-LR are both rapidly warming models with high ECS and TCR in CMIP6 (Meehl et al., 2020), meaning the amount of surface warming for a doubling of CO_2 in the atmosphere is relatively large, and happens quickly compared with other models. It is logical to expect that models with lower ECS and TCR would have a later TOE. Based on analysis of feedback processes, the historical record, and the paleoclimate record Sherwood et al. (2020) estimate that the true ECS is likely lower than is produced by CESM2 and IPSL-CM6A-LR.

To investigate the model dependence of TOE, we created synthetic MISR WCTH time series combining MISR output from AMIP simulations, with temperature data from SSP5-8.5 simulations (from models that performed the SSP5-8.5 experiment, but did not produce MISR output for this run) and a Fixed-Anvil-Temperature assumption. In effect, the MISR simulated cloud profile found in the AMIP run remains fixed with temperature and shifts up to maintain the same mean temperature in the SSP5-8.5 simulation. The synthetic WCTH projections showed that, as expected, models that experience more warming also tend to have faster rising cloud tops. However this does not consistently lead to an earlier TOE. Rather, between the slower rate of increase in CTH in slower-warming models, and the spread in TOE between models with similar rates of warming, it is possible that a MISR detection of any trends in the Tropics or Northern Hemisphere CTH could be as much as 5 years further out than suggested by the analysis in Section 3.

A major assumption in the present work is that biases in the climatological base state of the models, including biases in WCTH, are not important for the assessment of trend detection. There are notable biases in the model simulated cloud occurrence histograms (which are detailed in the supplementary materials). It is noteworthy that the apparent slope in WCTH is very similar between CESM2 and IPSL, and matches well the observations in at least the southern hemisphere (see bottom panels of **Figure 5**), in spite of the very different biases in the two models. Nonetheless, it remains an open area of study to determine if and how much base state differences of the models might influence the climate simulations, including the CTH trends.

Unfortunately, the TERRA satellite which houses the MISR instrument is running low on fuel and as of April 2021 the satellite has begun drifting from its fixed Equator Crossing Time (ECT). Diurnal variations in CTH will eventually cause an apparent change in CTH that is significant compared to that expected from climate change (shown in **Supplementary Figure S4**). When and how the orbit drifts will occur and how this will impact the ECT will have to be examined as part of future studies. Moving forward, NASA as part of the Aerosol, Cloud, Convection and Precipitation (ACCP) mission, plans to include a new stereo-imaging instrument which will make significantly more accurate measurements of cloud CTH than MISR. So, while there is likely to be a gap in the data record (and orbital differences will need to be considered carefully) there is hope that a long term, stereo-imaging, and calibration insensitive, data record on high cloud CTH will continue and will be able to constrain climate models. Even a continued negative signal in the tropics and NH (meaning non-detection of a change in CTH) should provide an upper bound on the possible rate of change.

Acknowledgments

This research was supported by the MISR project at the NASA Jet Propulsion Laboratory (under contract no. 1318945). We wish to acknowledge and thank the many modelling centers who contributed data to the Coupled Model Intercomparison Project that was necessary for this study, specifically A. Feofilov from LMD for running the IPSL model simulations, as well as Catherine Moroney, Steve Protack and everyone at NASA JPL and LaRC who produce the MISR CTH-OD data. Author Brian Medeiros acknowledges support by the U.S. Department of Energy under Award Number DE-SC0022070 and National Science Foundation (NSF) IA 1947282; the National Center for Atmospheric Research, which is a major facility sponsored by the NSF under Cooperative Agreement No. 1852977; and the National Oceanic and Atmospheric Administration under award NA20OAR4310392.

The MISR CTH-OD data can be obtained from the NASA Langley Research Center Atmospheric Sciences Data (DOI:10.5067/TERRA/MISR/MIL3MCOD.001). Additional details on obtaining observed and model simulated MISR CTH-OD datasets are given at the end of Section 2.

References

Aerenson, T. (2021). When Will MISR Detect Rising High Clouds? *Master of Science Thesis University of Washington*.

Bodas-Salcedo, A., Webb, M. J., Bony, S., Chepfer, H., Dufresne, J. L., Klein, S. A., … John, V. O. (2011). COSP: Satellite simulation software for model assessment. *Bulletin of the American Meteorological Society*, *92*(8), 1023–1043. https://doi.org/10.1175/2011BAMS2856.1

Bony, S., Stevens, B., Coppin, D., Becker, T., Reed, K. A., Voigt, A., & Medeiros, B. (2016). Thermodynamic control of anvil cloud amount. *Proceedings of the National Academy of Sciences of the United States of America*, *113*(32), 8927–8932. https://doi.org/10.1073/pnas.1601472113

Boucher, O., Servonnat, J., Albright, A. L., Aumont, O., Balkanski, Y., Bastrikov, V., … Vuichard, N. (2020). Presentation and Evaluation of the IPSL-CM6A-LR Climate Model.

Journal of Advances in Modeling Earth Systems, *12*(7), e2019MS002010. https://doi.org/10.1029/2019MS002010

Chepfer, H., Noel, V., Chiriaco, M., Wielicki, B., Winker, D., Loeb, N., & Wood, R. (2018). The Potential of a Multidecade Spaceborne Lidar Record to Constrain Cloud Feedback. *Journal of Geophysical Research: Atmospheres*, *123*(10), 5433–5454. https://doi.org/10.1002/2017JD027742

Chepfer, H., Noel, V., Winker, D., & Chiriaco, M. (2014). Where and when will we observe cloud changes due to climate warming'. *Geophysical Research Letters*, *41*(23), 8387–8395. https://doi.org/10.1002/2014GL061792

Danabasoglu, G., Lamarque, J. F., Bacmeister, J., Bailey, D. A., DuVivier, A. K., Edwards, J., … Strand, W. G. (2020). The Community Earth System Model Version 2 (CESM2). *Journal of Advances in Modeling Earth Systems*, *12*(2), e2019MS001916. https://doi.org/10.1029/2019MS001916

Davies, R., Jovanovic, V. M., & Moroney, C. M. (2017). Cloud heights measured by MISR from 2000 to 2015. *Journal of Geophysical Research*, *122*(7), 3975–3986. https://doi.org/10.1002/2017JD026456

Diner, D. J., Beckert, J. C., Reilly, T. H., Bruegge, C. J., Conel, J. E., Kahn, R. A., … Verstraete, M. M. (1998). Multi-angle imaging spectroradiometer (MISR) instrument description and experiment overview. *IEEE Transactions on Geoscience and Remote Sensing*, *36*(4), 1072–1087. https://doi.org/10.1109/36.700992

Gates, W. L., Boyle, J. S., Covey, C., Dease, C. G., Doutriaux, C. M., Drach, R. S., … Williams, D. N. (1999). An Overview of the Results of the Atmospheric Model Intercomparison Project (AMIP I). *Bulletin of the American Meteorological Society*, Vol. 80, pp. 29–55. https://doi.org/10.1175/1520-0477(1999)080<0029:AOOTRO>2.0.CO;2

Geiss, A., & Marchand, R. (2019). Cloud responses to climate variability over the extratropical oceans as observed by MISR and MODIS. *Atmospheric Chemistry and Physics*, *19*(11), 7547–7565. https://doi.org/10.5194/acp-19-7547-2019

Hansen, J. (1984). Climate sensitivity: analysis of feedback mechanisms. *Climate Processes and Climate Sensitivity*, 130–163. https://doi.org/10.1029/GM029p0130

Harrop, B. E., & Hartmann, D. L. (2012). Testing the role of radiation in determining tropical cloud-top temperature. *Journal of Climate*, *25*(17), 5731–5747. https://doi.org/10.1175/JCLI-D-11-00445.1

Hartmann, D. L., & Larson, K. (2002). An important constraint on tropical cloud - climate feedback. *Geophysical Research Letters*, *29*(20), 12-1-12–14. https://doi.org/10.1029/2002gl015835

Hillman, B. R., Marchand, R. T., Ackerman, T. P., Mace, G. G., & Benson, S. (2017). Assessing the accuracy of MISR and MISR-simulated cloud top heights using CloudSat- and CALIPSO-retrieved hydrometeor profiles. *Journal of Geophysical Research*, *122*(5), 2878–2897. https://doi.org/10.1002/2016JD025510

Hu, S., & Vallis, G. K. (2019). Meridional structure and future changes of tropopause height and temperature. *Quarterly Journal of the Royal Meteorological Society*, *145*(723), 2698–2717. https://doi.org/10.1002/qj.3587

Jeevanjee, N., & Fueglistaler, S. (2020). Simple spectral models for atmospheric radiative cooling. *Journal of the Atmospheric Sciences*, *77*(2), 479–497. https://doi.org/10.1175/JAS-D-18-0347.1

Kuang, Z., & Hartmann, D. L. (2007). Testing the fixed anvil temperature hypothesis in a cloud-

resolving model. *Journal of Climate*, *20*(10), 2051–2057. https://doi.org/10.1175/JCLI4124.1

Marchand, R. (2013). Trends in ISCCP, MISR, and MODIS cloud-top-height and optical-depth histograms. *Journal of Geophysical Research Atmospheres*, *118*(4), 1941–1949. https://doi.org/10.1002/jgrd.50207

Marchand, R., & Ackerman, T. (2010). An analysis of cloud cover in multiscale modeling framework global climate model simulations using 4 and 1 km horizontal grids. *Journal of Geophysical Research Atmospheres*, *115*(16), D16207. https://doi.org/10.1029/2009JD013423

Marchand, R., Ackerman, T., Smyth, M., & Rossow, W. B. (2010). A review of cloud top height and optical depth histograms from MISR, ISCCP, and MODIS. *Journal of Geophysical Research Atmospheres*, *115*(16), D16206. https://doi.org/10.1029/2009JD013422

Marchand, R. T., Ackerman, T. P., & Moroney, C. (2007). An assessment of Multiangle Imaging Spectroradiometer (MISR) stereo-derived cloud top heights and cloud top winds using ground-based radar, lidar, and microwave radiometers. *Journal of Geophysical Research Atmospheres*, *112*(6), D06204. https://doi.org/10.1029/2006JD007091

Meehl, G. A., Senior, C. A., Eyring, V., Flato, G., Lamarque, J. F., Stouffer, R. J., … Schlund, M. (2020). Context for interpreting equilibrium climate sensitivity and transient climate response from the CMIP6 Earth system models. *Science Advances*, Vol. 6. https://doi.org/10.1126/sciadv.aba1981

Mitra, A., Di Girolamo, L., Hong, Y., Zhan, Y., & Mueller, K. J. (2021). Assessment and Error Analysis of Terra-MODIS and MISR Cloud-Top Heights Through Comparison With ISS-CATS Lidar. *Journal of Geophysical Research: Atmospheres*, *126*(9), e2020JD034281. https://doi.org/10.1029/2020JD034281

Moroney, C., Davies, R., & Muller, J. P. (2002). Operational retrieval of cloud-top heights using MISR data. *IEEE Transactions on Geoscience and Remote Sensing*, *40*(7), 1532–1540. https://doi.org/10.1109/TGRS.2002.801150

Mueller, K. J., Wu, D. L., Horváth, Á., Jovanovic, V. M., Muller, J. P., Girolamo, L. Di, … Wanzong, S. (2017). Assessment of MISR Cloud Motion Vectors (CMVs) relative to GOES and MODIS Atmospheric Motion Vectors (AMVs). *Journal of Applied Meteorology and Climatology*, *56*(3), 555–572. https://doi.org/10.1175/JAMC-D-16-0112.1

Norris, J. R., Allen, R. J., Evan, A. T., Zelinka, M. D., O'Dell, C. W., & Klein, S. A. (2016). Evidence for climate change in the satellite cloud record. *Nature*, *536*(7614), 72–75. https://doi.org/10.1038/nature18273

O'Neill, B. C., Tebaldi, C., Van Vuuren, D. P., Eyring, V., Friedlingstein, P., Hurtt, G., … Sanderson, B. M. (2016). The Scenario Model Intercomparison Project (ScenarioMIP) for CMIP6. *Geoscientific Model Development*, *9*(9), 3461–3482. https://doi.org/10.5194/gmd-9-3461-2016

Rossow, W. B., Walker, A. W., & Garder, L. C. (1993). Comparison of ISCCP and other cloud amounts. *Journal of Climate*, *6*(12), 2394–2418. https://doi.org/10.1175/1520-0442(1993)006<2394:COIAOC>2.0.CO;2

Saint-Lu, M., Bony, S., & Dufresne, J. L. (2020). Observational Evidence for a Stability Iris Effect in the Tropics. *Geophysical Research Letters*, *47*(14), e2020GL089059. https://doi.org/10.1029/2020GL089059

Schneider, S. H. (1972). Cloudiness as a Global Climatic Feedback Mechanism: The Effects on the Radiation Balance and Surface Temperature of Variations in Cloudiness. *Journal of the*

Atmospheric Sciences, *29*(8), 1413–1422. https://doi.org/10.1175/1520-0469(1972)029<1413:caagcf>2.0.co;2

Seeley, J. T., Jeevanjee, N., & Romps, D. M. (2019). FAT or FiTT: Are Anvil Clouds or the Tropopause Temperature Invariant? *Geophysical Research Letters*, *46*(3), 1842–1850. https://doi.org/10.1029/2018GL080096

Séférian, R., Nabat, P., Michou, M., Saint-Martin, D., Voldoire, A., Colin, J., … Madec, G. (2019). Evaluation of CNRM Earth System Model, CNRM-ESM2-1: Role of Earth System Processes in Present-Day and Future Climate. *Journal of Advances in Modeling Earth Systems*, *11*(12), 4182–4227. https://doi.org/10.1029/2019MS001791

Sherwood, S. C., Webb, M. J., Annan, J. D., Armour, K. C., Forster, P. M., Hargreaves, J. C., … Zelinka, M. D. (2020, December 25). An Assessment of Earth's Climate Sensitivity Using Multiple Lines of Evidence. *Reviews of Geophysics*, Vol. 58. https://doi.org/10.1029/2019RG000678

Soden, B. J., & Held, I. M. (2006). An assessment of climate feedbacks in coupled ocean-atmosphere models. *Journal of Climate*, *19*(14), 3354–3360. https://doi.org/10.1175/JCLI3799.1

Stephens, G. L. (2005, January 15). Cloud feedbacks in the climate system: A critical review. *Journal of Climate*, Vol. 18, pp. 237–273. https://doi.org/10.1175/JCLI-3243.1

Swales, D. J., Pincus, R., & Bodas-Salcedo, A. (2018). The Cloud Feedback Model Intercomparison Project Observational Simulator Package: Version 2. *Geoscientific Model Development*, *11*(1), 77–81. https://doi.org/10.5194/gmd-11-77-2018

Swart, N. C., Cole, J. N. S., Kharin, V. V., Lazare, M., Scinocca, J. F., Gillett, N. P., … Winter, B. (2019). The Canadian Earth System Model version 5 (CanESM5.0.3). *Geoscientific Model Development*, *12*(11), 4823–4873. https://doi.org/10.5194/gmd-12-4823-2019

Takahashi, H., Lebsock, M. D., Richardson, M., Marchand, R., & Kay, J. E. (2019). When Will Spaceborne Cloud Radar Detect Upward Shifts in Cloud Heights? *Journal of Geophysical Research: Atmospheres*. https://doi.org/10.1029/2018JD030242

Tebaldi, C., Debeire, K., Eyring, V., Fischer, E., Fyfe, J., Friedlingstein, P., … Ziehn, T. (2020). Climate model projections from the Scenario Model Intercomparison Project (ScenarioMIP) of CMIP6. *Earth System Dynamics Discussions*, 1–50. https://doi.org/10.5194/esd-2020-68

Thompson, D. W. J., Bony, S., & Li, Y. (2017). Thermodynamic constraint on the depth of the global tropospheric circulation. *Proceedings of the National Academy of Sciences of the United States of America*, *114*(31), 8181–8186. https://doi.org/10.1073/pnas.1620493114

Vaillant de Guélis, T., Chepfer, H., Guzman, R., Bonazzola, M., Winker, D. M., & Noel, V. (2018). Space lidar observations constrain longwave cloud feedback. *Scientific Reports*, *8*(1), 1–8. https://doi.org/10.1038/s41598-018-34943-1

Vallis, G. K., Zurita-Gotor, P., Cairns, C., & Kidston, J. (2015). Response of the large-scale structure of the atmosphere to global warming. *Quarterly Journal of the Royal Meteorological Society*, *141*(690), 1479–1501. https://doi.org/10.1002/qj.2456

Voldoire, A., Saint-Martin, D., Sénési, S., Decharme, B., Alias, A., Chevallier, M., … Waldman, R. (2019). Evaluation of CMIP6 DECK Experiments With CNRM-CM6-1. *Journal of Advances in Modeling Earth Systems*, *11*(7), 2177–2213. https://doi.org/10.1029/2019MS001683

Webb, M. J., Andrews, T., Bodas-Salcedo, A., Bony, S., Bretherton, C. S., Chadwick, R., … Watanabe, M. (2017). The Cloud Feedback Model Intercomparison Project (CFMIP) contribution to CMIP6. *Geoscientific Model Development*, *10*(1), 359–384.

https://doi.org/10.5194/gmd-10-359-2017

Wetherald, R. T., & Manabe, S. (1988). Cloud feedback processes in a general circulation model. *Journal of the Atmospheric Sciences*, *45*(8), 1397–1415. https://doi.org/10.1175/1520-0469(1988)045<1397:CFPIAG>2.0.CO;2

Wilks, D. S. (1997). Resampling hypothesis tests for autocorrelated fields. *Journal of Climate*, *10*(1), 65–82. https://doi.org/10.1175/1520-0442(1997)010<0065:RHTFAF>2.0.CO;2

Wu, T., Lu, Y., Fang, Y., Xin, X., Li, L., Li, W., … Liu, X. (2019). The Beijing Climate Center Climate System Model (BCC-CSM): The main progress from CMIP5 to CMIP6. *Geoscientific Model Development*, *12*(4), 1573–1600. https://doi.org/10.5194/gmd-12-1573-2019

Yukimoto, S., Kawai, H., Koshiro, T., Oshima, N., Yoshida, K., Urakawa, S., … Ishii, M. (2019). The meteorological research institute Earth system model version 2.0, MRI-ESM2.0: Description and basic evaluation of the physical component. *Journal of the Meteorological Society of Japan*, *97*(5), 931–965. https://doi.org/10.2151/jmsj.2019-051

Zelinka, M. D., & Hartmann, D. L. (2010). Why is longwave cloud feedback positive? *Journal of Geophysical Research Atmospheres*, *115*(16). https://doi.org/10.1029/2010JD013817

Zelinka, M. D., Klein, S. A., Taylor, K. E., Andrews, T., Webb, M. J., Gregory, J. M., & Forster, P. M. (2013). Contributions of different cloud types to feedbacks and rapid adjustments in CMIP5. *Journal of Climate*, *26*(14), 5007–5027. https://doi.org/10.1175/JCLI-D-12-00555.1

Zelinka, M. D., Myers, T. A., McCoy, D. T., Po-Chedley, S., Caldwell, P. M., Ceppi, P., … Taylor, K. E. (2020). Causes of Higher Climate Sensitivity in CMIP6 Models. *Geophysical Research Letters*, *47*(1). https://doi.org/10.1029/2019GL085782

Zhou, C., Dessler, A. E., Zelinka, M. D., Yang, P., & Wang, T. (2014). Cirrus feedback on interannual climate fluctuations. *Geophysical Research Letters*, *41*(24), 9166–9173. https://doi.org/10.1002/2014GL062095